UNIVERSITÉ DE MONTRÉAL

NUMERICAL ANALYSIS OF A CONICAL TYPE COAXIAL OPEN-ENDED PROBE FOR DIELECTRIC MEASUREMENT

HOMA ARAB SALMANABADI
DÉPARTEMENT DE GÉNIE ÉLECTRIQUE
ÉCOLE POLYTECHNIQUE DE MONTRÉAL

MÉMOIRE PRÉSENTÉ EN VUE DE L'OBTENTION
DU DIPLÔME DE MAÎTRISE ÈS SCIENCES APPLIQUÉES
(GÉNIE ÉLECTRIQUE)
JUILLET 2014

UNIVERSITÉ DE MONTRÉAL

ÉCOLE POLYTECHNIQUE DE MONTRÉAL

Ce mémoire intitulé:

NUMERICAL ANALYSIS OF A CONICAL TYPE COAXIAL OPEN-ENDED PROBE FOR DIELECTRIC MEASUREMENT

présenté par: ARAB SALMANABADI Homa
en vue de l'obtention du diplôme de: Maîtrise ès sciences appliquées
a été dûment accepté par le jury d'examen constitué de:

M. WU Ke, Ph.D., président
M. AKYEL Cevdet, Ph.D., membre et directeur de recherche
M. CONAN Jean, Ph.D., membre et codirecteur de recherche
M. LAURIN Jean-Jacques, Ph.D., membre

ACKNOWLEDGEMENTS

I am heartily thankful to my supervisor, professor Akyel, whose encouragement, guidance and support from the initial to the final level enabled me to develop an understanding of the subject. I owe my deepest gratitude to Professor Conan, for his support and helpful suggestions. I would like to thank Dr. Xu for the extra time and grateful contributions he has given throughout the course of this work. Also, I offer my regards and blessings to all of those who supported me in any respect during the completion of the project. All of your help will not be forgotten.

Last but not the least, this thesis is dedicated to my parents for their endless support and encouragement.

RÉSUMÉ

L'objectif principal de cette recherche est de trouver un modèle précis pour le calcul de la constante diélectrique et le facteur de perte d'un matériau diélectrique homogène à partir d'un coefficient de réflexion mesurée à l'aide d'une sonde coaxiale de type conique dans les fréquences radio et micro-ondes. Ce type de sonde peut être facilement inséré dans plusieurs types de tissus biologiques et dans des matériaux semi-rigides comme le caoutchouc, certains plastiques et des matières organiques (ex.: des produits laitiers comme le beurre, pour en mesurer la teneur en humidité). Cette caractéristique est très importante pour des applications biologiques et industrielles. Le principe à la base de ce type de mesure est la détection de la variation de capacité par rapport au mouvement de la masse diélectrique dans le champ de frange électrique. L'admittance d'entrée électrique, ainsi que le coefficient de réflexion, sont calculés à l'aide d'une analyse par éléments finis. Contrairement à de nombreuses autres techniques de modélisation utilisées pour l'étude des sondes coaxiales qui sont approximatives et donc limitées, le modèle par éléments finis est plus précis et est applicable aux géométries complexes. Afin de valider le modèle numérique, une étude expérimentale a été menée en parallèle en laboratoire, avec mêmes dimensions géométriques. Les résultats sont comparés et une excellente correspondance est observée, ce qui démontre que la modélisation par éléments finis est une bonne approche pour la conception optimale de sondes coaxiales coniques. Une formulation éléments finis tridimensionnelle est utilisée dans la région du matériau diélectrique et dans une petite région voisine de la structure de la sonde sur laquelle elle est montée. Le coefficient du facteur de réflexion, le champ électromagnétique à l'ouverture de la sonde et la permittivité de différents matériaux ont été analysés pour des fréquences de 300 MHz à 3 GHz. De plus, une étude comparative de trois modèles de sondes coniques à ouverture coaxiale (modèle capacitif, modèle d'antenne et modèle amélioré de la ligne virtuelle) qui fait un lien entre le coefficient de réflexion à la permittivité complexe du matériau testé est présentée. L'influence de l'angle du cône et de la forme du câble coaxial (plat-conique-elliptique) est aussi étudiée en détail. La conception de sondes diélectriques ainsi que leur utilisation efficace nécessite des méthodes de calcul précises et optimales, validées de façon rigoureuse et à coûts de calculs réduits.

ABSTRACT

The main objective of this research is to find an accurate model for computing the dielectric constant and the loss factor of a homogeneous dielectric material from a measured reflection coefficient by using conical-type coaxial probe in radio and microwave frequencies. This sort of probe can be easily inserted into a wide range of biological tissue types and semi-rigid materials like rubber, some plastics, and organic materials (e.g., dairy, butter, etc.) for measuring moisture content. This feature is very important in biological and industrial applications. The measuring principle is based on detecting capacitance change with respect to the dielectric mass movement in the fringe electrical field. The electrical input admittance as well as the reflection coefficient are found from the finite-element analysis. In contrast to many other modelling techniques used for coaxial probe which are approximate and hence limited, the finite-element model is more accurate and is applicable to complicated geometries. To demonstrate the accuracy of the numerical model, a parallel experimental study was carried out in the laboratory in the same geometric dimensions. The numerical and experimental results are compared and showed an excellent agreement, demonstrating that finite-element modelling is a good approach for optimized conical coaxial probe design. A three-dimensional finite-element formulation is employed in the dielectric material region and a small neighbouring region of the probe structure on which it is mounted. The reflection coefficient factor, electromagnetic field at the probe aperture and permittivity of different materials were analyzed in the frequency range of 300 MHz to 3 GHz. Moreover, a comparative study of three conical open-ended coaxial probe models (capacitive model, antenna model, improved virtual line model) which relate the reflection coefficient to the complex permittivity of the Material Under Test (MUT) is presented. In addition, the effects of the cone angle and shape of the coaxial cable (flat-conical-elliptical) are studied and evaluated in detail in this research. It is shown that for designing an efficient and operational dielectric measurement probe, an accurate and computationally efficient method with rigorous validation and reduced computational burden is required.

CONTENTS

LIST OF TABLES

LIST OF FIGURES

ABBREVIATIONS

E	Electric field strength
D	Displacement field strength
H	Magnetic field strength
B	Magnetic flux density
J	Electric current density
P	Electric polarization vector
M	Magnetization vector
Π_e	Electric vector potential
Π_m	Magnetic vector potential
Ω	Electric scalar potential
Φ	Magnetic scalar potential
ρ	Electric charge density
ϵ_r	Relative permittivity
μ_r	Relative permeability
σ	Electric conductivity
t	Time
ω	Angular frequency
$tan(\delta)$	loss (dissipation) factor
C	Capacitance (F)
G	Conductance
S-parameter	Scattering parameter
S_{11}	Reflection coefficient at measurement port
$\overline{S_{11}}$	Reflection coefficient at aperture port
MUT	Material under test
TE	Transversal electric mode
TM	Transversal magnetic mode
TEM	Transversal electric and magnetic wave
FEM	Finite element method
FDM	Finite-difference method

CHAPTER 1

INTRODUCTION

Measurement of dielectric properties of materials at microwave frequencies has been the subject of many researches in the publications [1–5]. The dielectric constant is a unique and essential property of dielectric materials to characterize the interaction between an electric field and matter. Accurate measurements of these properties can provide scientists and engineers with essential and valuable information to properly incorporate the materials into their intended applications. For example, this information is useful in the area of aerospace, automotive, agriculture, food engineering, bioengineering, medical treatments, and electronics applications, etc.

The interaction between the electrical and magnetic fields is described by the Maxwell equations. Basically, there are two ways to solve this system of equations: analytical and numerical methods. Unfortunately, analytical solutions developed and structured only for limited class of problems involving simple two-dimensional geometries, linear media and steady state problems. Three dimensional, non-linear and transient type problems are very difficult to solve analytically and limited solution algorithms exist only for specific problems. The current restrictions of complexity and accuracy in analytical methods can be overcome by using numerical techniques in electromagnetic devices having a complex geometry along with different material properties, especially those associated with close proximity and irregular space distribution. Numerical and successive/iterative/recurrent methods can handle non-uniform asymmetrical geometrical configurations, time-dependent problems and non-linear materials, different excitations and multiple materials [6, 7].

There are several numerical methods: the finite difference method, the finite element method, the finite-volume method, the finite integration technique, the boundary element method, the method of moments, and so on. The finite element method (FEM) is well adapted to deal with this class of problems, due to its flexibility for handling complex geometries. The equations are discretized using edge elements which enforces the tangential continuity of the vector fields, but not that of the normal components. Because of this, only the essential continuity properties of the electric field intensity are fulfilled when using edge elements.

There are many techniques that have been developed to characterization materials like the transmission/reflection line, open-ended coaxial probe, free space and resonator method(cavity method)[4, 5, 8]. The open-ended coaxial probe has been widely researched over the years

as a way to effectively and quickly characterize material properties in broad frequency bands (200MHz to near 50GHz). It is considered a very appealing characterization method, since the set-up time for a measurement is very short and the measurement is simple, convenient and non-destructive to the material. It is the best method for liquids or semi-solid materials[9, 10]. The open-ended coaxial probe is a cut off section of transmission line. The material is measured by immersing the probe into a liquid or touching the surface of a semi-solid or liquid materials. The fields at the probe end fringe into the material and change as they come into contact with the MUT. The reflected signal (S_{11}) can be measured and related to ϵ_r.

Many models have been built to analyze open ended coaxial probes terminated by semi-infinite homogeneous materials. There are three typical models (capacitive model, antenna model, and modified virtual line model)[11–13]. The accuracy of these three models in measuring lossy dielectric constant of materials are investigated. To the best of our knowledge, there is no study available in the literature to evaluate these models for conical type type coaxial probe. Infact, there is an undiscovered area in this field, that includes the study of conical type open ended coaxial line which is a coaxial line ending in a conical shape geometry. The advantage of this kind of probe is the possibility of placing the probe into the biological tissue types and semi-rigid materials which is difficult for the flat coaxial probe. In this research, we present a comparative study of three conical type open-ended coaxial probe models which relate the conical type coaxial probe reflection coefficient to the complex permittivity of the material under test. Then we investigate the sensitivity and accuracy of the models in measuring lossy dielectric for biological materials.

The contribution of this thesis are as follows:

1. Calculation of the electric field at the aperture of conical probe and consequently reflection coefficient by using finite element method.

2. Studying the three different conical-type open-ended coaxial probe models (capacitive-Antenna-Virtual Line) and finding the best model to relate the coaxial line end impedance to the complex permittivity of the material under test.

3. Considering the effect of different cone angles of conical coaxial probe on complex dielectric measurement.

4. Comparative study of different structure of probes (Flat-Conical-Elliptical)in complex dielectric measurement.

We believe that our present results are new and are not presently available in the literatures.

This short chapter is a brief introduction to the reader. In Chapter 2, the theoretical

principles are being presented and Maxwell equations are reformulated in terms of potentials. Potentials are auxiliary functions that express various physical properties in ways leading to a more workable solution to a problem involving Partial Differential Equations (PDE). In Chapter 3, the problems are solved by using a numerical method. The Finite Element Method (FEM) is well adapted to deal with this class of problems, due to its flexibility for handling complex geometries. The three-dimensional analysis by using the Comsol software is presented in this chapter. Chapter 4 presents the methods, models and algorithms that have been used to relate the coaxial line end impedance to the complex permittivity of the material under test. In Chapter 5, the measurement system and experimental results are presented. In it we study the handmade probes with different characteristics and angles. The measurements are done for four different liquids: water, methanol, butanol, and propanol. Moreover, the results of the measurement of the permittivity and the reflection coefficient of the system consisting of probes placed in liquids, and comparison between these results and those of which are obtained numerically and analytically are presented. The conclusions and contribution of this thesis are summarized in Chapter 6, followed by some future works given in Chapter 7.

CHAPTER 2

THEORETICAL STUDY OF THE COAXIAL-LINE CONICAL-TYPE PROBE

In this chapter, we briefly present a introductory theoretical method for solving wave equation analyticaly for open ended coaxial probes.

2.1 Electromagnetic Field Equations

The problem of electromagnetic field analysis on a macroscopic level is fully described by Maxwell equations subject to certain boundary conditions:

$$\nabla \times \mathbf{H} = \mathbf{J} + \frac{\partial \mathbf{D}}{\partial t}; \tag{2.1}$$

$$\nabla \times \mathbf{E} = -\frac{\partial \mathbf{B}}{\partial t}; \tag{2.2}$$

$$\nabla \cdot \mathbf{D} = \rho; \tag{2.3}$$

$$\nabla \cdot \mathbf{B} = 0, \tag{2.4}$$

where $\mathbf{E}$ is the electric field intensity, $\mathbf{H}$ is the magnetic field intensity, $\mathbf{D}$ is the electric displacement or electric flux density, $\mathbf{J}$ is the current density, and ρ is the electric charge density. The constitutive relations describing the macroscopic properties of the medium are given as:

$$\mathbf{D} = \varepsilon \mathbf{E}; \tag{2.5}$$

$$\mathbf{B} = \mu \mathbf{H}; \tag{2.6}$$

$$\mathbf{J} = \sigma \mathbf{E}. \tag{2.7}$$

The phasor form of equation can be derived from a time-dependent equation(replacing time variation by $j\omega$). The complex dielectric constant $\varepsilon = \varepsilon_0(\varepsilon_r' - j\varepsilon_r'')$ describes the interaction of a material with an electric field $\mathbf{E}$ and consists of a real part ε_r' which represents the storage of energy and an imaginary part ε_r'' which represents the loss of energy (both dielectric loss and conductivity). Here ε_0 is the permittivity of vacuum ($8.854 \times 10^{-12} F/m$) and μ_0 is the

permeability of vacuum ($4\pi \times 10^{-7} H/m$). Taking the curl of the curl equations gives:

$$\nabla \times \mu_r^{-1}(\nabla \times \mathbf{E}) - k_0^2(\epsilon_r - \frac{j\sigma}{\omega\epsilon_0})\mathbf{E} = 0; \tag{2.8}$$

$$\nabla \times \mu_r^{-1}(\nabla \times \mathbf{H}) - k_0^2(\epsilon_r - \frac{j\sigma}{\omega\epsilon_0})\mathbf{H} = 0, \tag{2.9}$$

where we defined $k_0 = \omega\sqrt{\mu_0\varepsilon_0}$ as the squared complex wave number. In this chapter a model of the coaxial probe is presented in Figure 2.1.

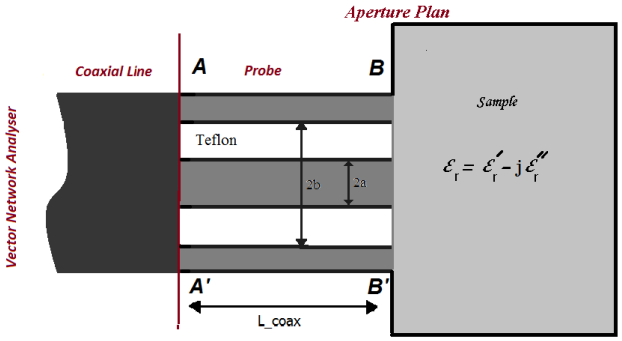

Figure 2.1: Cross-section view of the coaxial open-ended probe.

2.2 Hertz Potential

The electromagnetic field and electrostatic variables **H** and **E** can be solved directly, but it is often facilitated by the use of scalar and vector potentials. The potential describing decrease the solution of the Maxwell equations to the solution of different class of PDE equation. It was shown by Hertz that an arbitrary electromagnetic field in a (source free) homogeneous linear isotropic medium can be defined in terms of a single vector potential Π:

$$\nabla^2\mathbf{\Pi} + k^2\mathbf{\Pi} = 0, \tag{2.10}$$

where we defined $k = k_0^2(\epsilon_r + \frac{\sigma}{\omega\epsilon_r}j)$ as the squared complex wave number. Equation 2.10 has two types of independent solutions: $\mathbf{\Pi_m}$ and $\mathbf{\Pi_e}$. The zero divergence of **H** allows us to write **H** as the curl of a vector function, which result in independent sets of **E**-type waves:

$$\mathbf{H} = (\sigma + j\omega\epsilon)\nabla \times \mathbf{\Pi_e}; \tag{2.11}$$

$$\mathbf{E} = k^2\mathbf{\Pi_e} + \nabla(\nabla \cdot \mathbf{\Pi_e}), \tag{2.12}$$

and similarly the zero divergence of **E** leads to a solution of the **H**-type waves:

$$\mathbf{E} = j\omega\mu\nabla \times \mathbf{\Pi_m}; \tag{2.13}$$

$$\mathbf{H} = k^2\mathbf{\Pi_m} + \nabla(\nabla \cdot \mathbf{\Pi_m}). \tag{2.14}$$

Based on the Green's function for a dipole source the Hertzian potentials are:

$$\mathbf{\Pi_e} = \mathbf{P}_e \frac{e^{-jkr}}{r}; \tag{2.15}$$

$$\mathbf{\Pi_m} = \mathbf{P}_m \frac{e^{-jkr}}{r}; \tag{2.16}$$

$$\mathbf{Kdl} = \iint \mathbf{J}_{sm}\mathbf{da} = \iint \mathbf{E} \times \mathbf{da}; \tag{2.17}$$

$$\mathbf{P}_e = \frac{-j\mathbf{Idl}}{4\pi\omega\epsilon}; \quad \mathbf{P}_m = \frac{-j\mathbf{Kdl}}{4\pi\omega\mu}, \tag{2.18}$$

where $\mathbf{P}_e$ is the electric polarization vector, $\mathbf{P}_m$ is the magnetic polarization vector, $\mathbf{I}$ is the current, $\mathbf{l}$ is the electric dipole length vector, $\mathbf{K}$ is the current surface, $\mathbf{J_{sm}}$ is the magnetic surface current, and $\mathbf{a}$ is the loop area vector; therefore, the electric an magnetic potential are related to elementary electric and magnetic current by:

$$\mathbf{\Pi_e} = \frac{-j\mathbf{Idl}}{4\pi\omega\epsilon}\frac{e^{-jkr}}{r}; \tag{2.19}$$

$$\mathbf{\Pi_m} = \frac{-j\mathbf{Kdl}}{4\pi\omega\mu}\frac{e^{-jkr}}{r}; \tag{2.20}$$

$$\mathbf{Kdl} = \iint \mathbf{J}_{sm}da = \iint \mathbf{E} \times \mathbf{da}, \tag{2.21}$$

where the tangential electric field of the aperture is integrated over the area of the slot. The magnetic field inside and outside the coaxial probe are related to the tangential electric field of the aperture $E_r(r', \varphi')$ by:

$$d\mathbf{H} = \frac{2j}{4\pi\omega\mu}E_r(r', \varphi')(\nabla^2 + k^2)\frac{e^{-jkr}}{r}(\mathbf{j}_{r'} \times \mathbf{j}_z)r'dr'd\varphi'; \tag{2.22}$$

$$r = [r^2 + r'^2 - 2rr'cos(\varphi - \varphi') + z^2]^{1/2}. \tag{2.23}$$

The electric field is taken to be the principal mode and has only r component $E_r(r', \varphi'))$ and exhibit no variations in φ direction. The operator $\nabla = j_\varphi \frac{\partial}{\partial\varphi}$ equals zero, and consequently

∇^2 is zero. by substituting $\mathbf{j}_{r'} \times \mathbf{j}_z = -\mathbf{j}_\varphi$, the magnetic field is related to $E_r(r', \varphi')$ as:

$$\mathbf{H}_\varphi(r, \varphi, z) = \frac{k^2}{2\pi j\omega\mu} \int_a^b E_r(r', \varphi') r' dr' \int_0^{2\pi} \frac{e^{jkr}}{r} cos(\psi) d\psi, \tag{2.24}$$

where $\psi = \varphi - \varphi'$ and the last integration will be expressed in terms of Bessel functions [14].

2.3 Electromagnetic Fields in Cylindrical Coordinates

In cylindrical coordinates, the electric field can be decomposed into radial, azimuthal and longitudinal components. With this separation, the Helmholtz equations can be decomposed into separate equations for E_r, E_φ, E_z and H_r, H_φ, H_z. However, these three components are not completely independent. In fact, classic electromagnetic theory indicates that in cylindrical coordinate the transversal field components E_φ and H_r can be expressed as a combination of longitudinal field components E_r and H_φ. This means that electromagnetic fields can be derived from the φ component of magnetic field which is not independent of the φ [15]. In cylindrical coordinates, the Helmholtz equation for H_φ is:

$$\frac{\partial^2 H_\varphi}{\partial r^2} + \frac{1}{r}\frac{\partial H_\varphi}{\partial r} + \frac{\partial^2 H_\varphi}{\partial z^2} + k^2 H_\varphi = 0. \tag{2.25}$$

The r component of electric field is computed to be:

$$-j\omega\epsilon E_r(r, \varphi, z) = (\frac{\partial}{\partial r} + \frac{1}{r}) H_\varphi(r, \varphi, z). \tag{2.26}$$

And the boundary condition at aperture port (see Figure 2.1) defined by:

$$(\frac{\partial}{\partial r} + \frac{1}{r}) H_\varphi(r, \varphi, z) = 0 \quad r{=}a, b. \tag{2.27}$$

In accordance with the preceding section the general expression for φ component of magnetic field is:

$$H_\varphi(r, \varphi, z) = \frac{A_0}{r}(e^{jkz} - R_0 e^{-jkz}) + \Sigma_{n=1}^{\infty} A_n R_n(r) e^{(\lambda^2 - k^2)z}. \tag{2.28}$$

The first terms represent the incident TEM mode, the second term reflected TEM mode and the infinite series represent the higher-order modes. All the higher-order modes are exponentially damped with increasingly the value of z. The eigenfunctions $R_n(r)$ are defined

as:

$$(\frac{\partial^2}{\partial r^2}+\frac{1}{r}\frac{\partial}{\partial r}-\frac{1}{r^2}+\lambda^2)R_n(r)=0; \tag{2.29}$$

$$(\frac{\partial}{\partial r}+\frac{1}{r})R_n(r)=0 \quad at\ r{=}a,b; \tag{2.30}$$

$$R_n(r)=J_1(\lambda_n r)Y_0(\lambda_n a)-J_0(\lambda_n a)Y_1(\lambda_n r). \tag{2.31}$$

where **J** is the Bessel functions of the first kind and **Y** is the Bessel functions of the second kind [15]. The eigenvalues are roots of transcendental equation:

$$Y_0(\lambda_n a)J_0(\lambda_n b)=J_0(\lambda_n a)Y_0(\lambda_n b)], \tag{2.32}$$

and the second kind of the Bessel function order n (Y_n) is defined by:

$$Y_n=\frac{\sqrt{2}}{\pi\lambda_n}[\frac{J_0^2(\lambda_n a)}{J_0^2(\lambda_n b)}-1]^{1/2}. \tag{2.33}$$

By applying 2.31 to 2.26 , the r component of electric field is computed as:

$$j\omega\epsilon E_r(r,\varphi,z)=\frac{\partial}{\partial z}H_\varphi(r,\varphi,z)=\frac{ikA_0}{r}(e^{jkz}-jkR_0e^{-jkz})+\Sigma_{n=1}^{\infty}A_nR_n(r)(\lambda^2-k^2)^{1/2}e^{(\lambda^2-k^2)^{1/2}z}. \tag{2.34}$$

By setting $z=0$, multiplying two side by $rR_n(r,z)$ and by taking the integral over the surface of the aperture of the probe, we have:

$$A_n=\frac{i\omega\epsilon_i\int_s E_r(r,\varphi)R_n(r,\varphi)ds}{(\lambda^2-k^2)^{1/2}}, \tag{2.35}$$

and A_0 is:

$$A_0=\frac{\omega\epsilon_i\int_s E_r(r,\varphi)H_\varphi(r,\varphi)ds}{k(1+R_0)\int_s[H_\varphi(r,\varphi)]^2ds}. \tag{2.36}$$

The normalized admittance of coaxial probe is obtained by inserting 2.35 and 2.36 in 2.28, and the tangential magnetic field by using 2.28 is equal expression given in 2.24

$$\frac{\omega\epsilon(1+R_0)\int_s E_r(r,\varphi)H_\varphi(r,\varphi)ds}{k(1+R_0)\int_s[H_\varphi(r,z)]^2ds}+\Sigma_{n=1}^{\infty}\frac{i\omega\epsilon\int_s E_r(r,\varphi)R_n(r,\varphi)ds}{(\lambda^2-k^2)^{1/2}}R_n(r)e^{(\lambda^2-k^2)^{1/2}z}; \tag{2.37}$$

$$=\frac{2i}{4\pi\omega\mu}E_r(r',\varphi')(\nabla^2+k^2)\frac{e^{ikr}}{r}(\mathbf{i}_{r'}\times\mathbf{i}_z)ds, \tag{2.38}$$

which results in:

$$Y_s = \frac{1 - R_0}{1 + R_0} = \frac{i \int_s H_{\varphi 0}(r, \varphi) \int_{s1} E_{r1}(r_1, \varphi_1)(\nabla^2 + k^2) \frac{e^{ikr}}{r} cos(\psi) d\psi}{2\pi \sqrt{\epsilon} k_0 \int_s E_r(r, \varphi) H_{\varphi 0}(r, \varphi)}. \tag{2.39}$$

It is shown in different references [16], [17] that for any arbitrary function the first part of integral ∇^2 over the aperture of the coaxial line is equal to zero, and we have:

$$Y_s = \frac{i \int_s H_{\varphi 0}(r, \varphi) \int_{s1} E_{r1}(r_1, \varphi_1) \frac{e^{ikr}}{r} cos(\psi) d\psi}{2\pi \sqrt{\epsilon} k_0 \int_s E_r(r, \varphi) H_{\varphi 0}(r, \varphi)}, \tag{2.40}$$

where s_1 is the aperture surface and the electric field (E_r) and magnetic field (H_φ) components of the principal mode are related to metrical coefficient of the cylindrical coordinates ($h_r = 1$, $h_\varphi = r^2$, and $h_z = 1$). The derivation of this integral equation was explained in details in [16, 18, 19] The detailed description for solving Helmholtz equation in cylindrical coordination can be found in Appendices A.

For a conical type coaxial probe, the electric field in the aperture is not just a function of the radius (r) and the phase φ, and a new variable must be defined due to the geometry of the probe. However, in recent years, numerical methods have also been used to analyse open-ended coaxial lines and with easy access to fast computers, the tangential electric field of the aperture can be determined quickly and accurately. The electric and magnetic fields calculated by numerical methods are in good agreement with experimental results which will be discussed in next chapters.

CHAPTER 3

NUMERICAL STUDY OF COAXIAL-LINE THE CONICAL-TYPE COAXIAL PROBE

In this chapter, we present a numerical solution for solving the Helmholtz equation within the volume of the conical type coaxial probe and a small neighbouring region of the sample on which it is mounted.

3.1 Discretization of the formulation using the finite element method

Typically, a finite element solution is divided in the following steps: [20]

1. Understanding the physical problem (identifying the differential equation and its boundary conditions).
2. Element idealization (characterizing the finite element dimensionality 1D, 2D and 3D depending on the characterization of geometric beams, plate, solid, etc.)
3. Selection of the element type (in 1-D, 2-D (triangular or quadrilateral), or 3-D (tetrahedral, hexahedral, etc.), and may be linear or higher-order)
4. Selection of the type of analysis (weak formulation or functional minimizing)
5. Selection of the solution method (direct method or iterative method)
6. Solving the eigenvalue matrix form problem
7. Post-processing

The two classical methods for discretizing the wave equations in a conical coaxial probe in 2D are presented in next section [21, 22].

3.2 Solution with the Ritz method

In the Ritz method, we formulate the problem in term of a functional whose minimum corresponds to the differential equation under specific boundary conditions [21]. The variation

formulation for wave is:

$$F(\mathbf{E}) = \iint \mu^{-1}(\nabla \times \mathbf{E})(\nabla \times \mathbf{E})d\Omega - \iint k_0^2 \epsilon \mathbf{E} \cdot \mathbf{E}^* d\Omega; \tag{3.1}$$

$$n \times \mathbf{E} = 0, \qquad in \quad boundaries \quad \Omega \tag{3.2}$$

where Ω is the cross section coaxial probe which is presented in Figure 3.1.

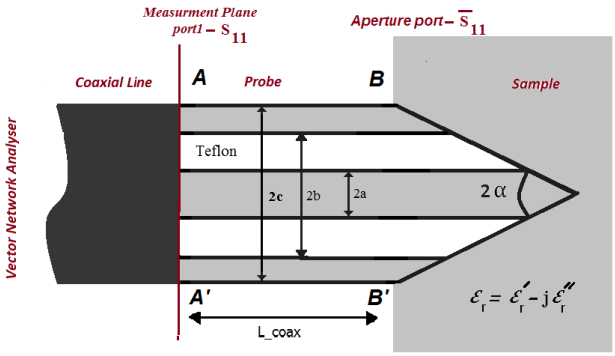

Figure 3.1: Cross-section view of the coaxial open-ended probe.

By assuming z is the direction of propagation we will have $E(x, y, z) = E(x, y)e^{-jk_z z}$ where k_z is the propagation constant, so equation 2.8 can be written as:

$$F(\mathbf{E}) = \iint \mu^{-1}(\nabla_t \times \mathbf{E}_t)(\nabla_t \times \mathbf{E}_t)d\Omega - k_0^2 \epsilon \mathbf{E}_t \cdot \mathbf{E}_t^* d\Omega + \cdots$$
$$\mu^{-1}(\nabla_t E_z + jk_z E_t) \cdot (\nabla_t E_z + jk_z E_t)^* d\Omega, \tag{3.3}$$

where ∇_t denotes the transverse del operator, E_t denotes the transverse component of the electric field, and E_z the z-component of the field. This functional can be discretized to yield an eigenvalue system that can be solved for k_0^2 for a given k_z. Based on FEM method, E can be approximated by the expansion:

$$E(x, y) = \sum_{j=1}^{n} N_j^e(x, y) E_j^e, \tag{3.4}$$

where $N_j^e(x, y)$ are the basis function defined over the entire domain, and n is the number of nodes in the element (for first order triangular element n equals to three), and E_j^e is constant coefficients to be determined.

3.3 Solution with the Galerkin method

The Galerkin method is very popular for finding numerical solutions to differential equations where the solution residue is minimized, giving rise to the well-known weak formulation of problems. The idea is to approximate the solution to a differential equation by very simple functions. In this section the system of equations is derived by using Galerkin method. For simplicty the residual associated with equation 2.8 in 2D is considered [21].

$$r = \frac{\partial}{\partial x}\mu_r^{-1}(\frac{\partial E}{\partial x}) + \frac{\partial}{\partial y}\mu_r^{-1}(\frac{\partial E}{\partial y}) - k_0^2\epsilon E; \tag{3.5}$$

$$R^e(E^e) = \iint_\Omega N_i^e r d\Omega; \tag{3.6}$$

$$R^e(E^e) = \iint_\Omega N_i^e\big(\frac{\partial}{\partial x}\mu_r^{-1}(\frac{\partial E}{\partial x}) + \frac{\partial}{\partial y}\mu_r^{-1}(\frac{\partial E}{\partial y}) - k_0^2\epsilon E\big)d\Omega. \tag{3.7}$$

Then invoking identities:

$$\mu_r^{-1}(\frac{\partial E}{\partial x})(\frac{\partial N_i}{\partial x}) = \frac{\partial}{\partial x}(\mu_r^{-1}\frac{\partial E}{\partial x}N_i) - (\frac{\partial}{\partial x}(\mu_r^{-1}\frac{\partial E}{\partial x})N_i, \tag{3.8}$$

and the divergence theorem

$$\iint_\Omega(\frac{\partial U}{\partial x} + \frac{\partial V}{\partial y})d\Omega = \oint_\Gamma(U\bar{i} + V\bar{j}).\overline{n}d\Gamma. \tag{3.9}$$

The equation 3.7 can be written:

$$R^e(E^e) = \iint_\Omega \mu_r^{-1}(\frac{\partial N_i^e}{\partial x})(\frac{\partial E}{\partial x}) + \mu_r^{-1}(\frac{\partial N_i^e}{\partial y})(\frac{\partial E}{\partial y})d\Omega - \iint_\Omega N_i^e \cdot k_0^2\epsilon E d\Omega$$
$$- \oint_\Gamma(\mu_r^{-1}\frac{\partial E}{\partial x}\bar{i} + \mu_r^{-1}\frac{\partial E}{\partial y}\bar{j}) \cdot \overline{n}d\Gamma, \tag{3.10}$$

where Γ denote the contour surrounding Ω and $\overline{n}$ is the outward unique vector. By substitution 3.4 into the above equation obtained:

$$R^e(A^e) = \sum_{i=1}^{3}\iint_\Omega \mu_r^{-1}(\frac{\partial N_i^e}{\partial x})(\frac{\partial N_j^e}{\partial x}) + \mu_r^{-1}(\frac{\partial N_i^e}{\partial y})(\frac{\partial N_j^e}{\partial y})d\Omega - k_0^2\varepsilon\iint_\Omega N_i^e \cdot N_j^e d\Omega$$
$$- \oint_\Gamma(\mu_r^{-1}\frac{\partial N_j^e}{\partial x}\bar{i} + \mu_r^{-1}\frac{\partial N_j^e}{\partial y}\bar{j}) \cdot \overline{n}d\Gamma. \tag{3.11}$$

We can now assemble the element equation for all M elements as

$$\{R\} = [K]\{\phi\} - [b] - [g], \tag{3.12}$$

where matrix $[K]$ is assembled from matrix $[K]^e$ and vector $\{b\}$ is assembled from vector $\{b\}^e$

$$[K] = \sum_{i=1}^{n} [K^e] \quad ; \quad [b] = \sum_{i=1}^{n} [b^e]. \tag{3.13}$$

We used the relation between the global and local node numbers.

$$\begin{cases} K^e = \iint_\Omega \left(\mu_r^{-1}(\frac{\partial N_i^e}{\partial x})(\frac{\partial N_j^e}{\partial x}) + \mu_r^{-1}(\frac{\partial N_i^e}{\partial y})(\frac{\partial N_j^e}{\partial y})\right) d\Omega \\ b^e = k_0^2 \varepsilon \iint_\Omega N_i^e \cdot N_j^e d\Omega \\ g^e = \oint\!\!\!\!\!\!- _\Gamma (\mu_r^{-1} \frac{\partial N_j^e}{\partial x} \bar{i} + \mu_r^{-1} \frac{\partial N_j^e}{\partial y} \bar{j}) \cdot \overline{n} d\Gamma \end{cases} \tag{3.14}$$

After discretization the functional and substituting nodal and edge element basic function (The details of the description for nodal and edge elements discretization can be found in Appendices B and C), we can obtain the generalized matrix form eigenvalue problem that can be solved with any iterative or direct method. More detail about this part can be found in [7, 21, 23]. The Matlab code related to this chapter can be found at the end of this document after references. In next section, we will solve the problem by using the Comsol Software which uses the same method.

3.4 Structure definition

The 3-dimensional electromagnetic structure of conical-type open-ended coaxial probe shown in Figure 3.2 is considered. The global constants related to structure and material properties are presented in Table 3.1. The probes are made by POLY-GRAMES technicians in the past.

Table 3.1 Global constant for electromagnetic model of the coaxial probe.

Name	Expression	Description
a	0.455 [mm]	Coax inner radius
b	1.49 [mm]	Coax outer radius
c	1.79 [mm]	Coax outer conductor
L_{coax}	250 [mm]	Length of coax core into cavity
f	300[MHz]-30[GHz]	Frequency
λ_0	$\frac{c_{const}}{f}$	Wavelength, air
h_{max}	$0.2\lambda_0$	Maximum mesh element size
Z_{coax}	$\frac{Z_{0const}}{2\pi\varepsilon_r} log(\frac{R_{coax}}{r_{coax}})$	Analytical impedance for flat coaxial Probe
α	30°	Cone Angle

For meshing, the toolbar of Comsol is used which exports the triangle vertices, triangle edges, and triangle ordering. The results of the meshing are illustrated in Figure 3.2.

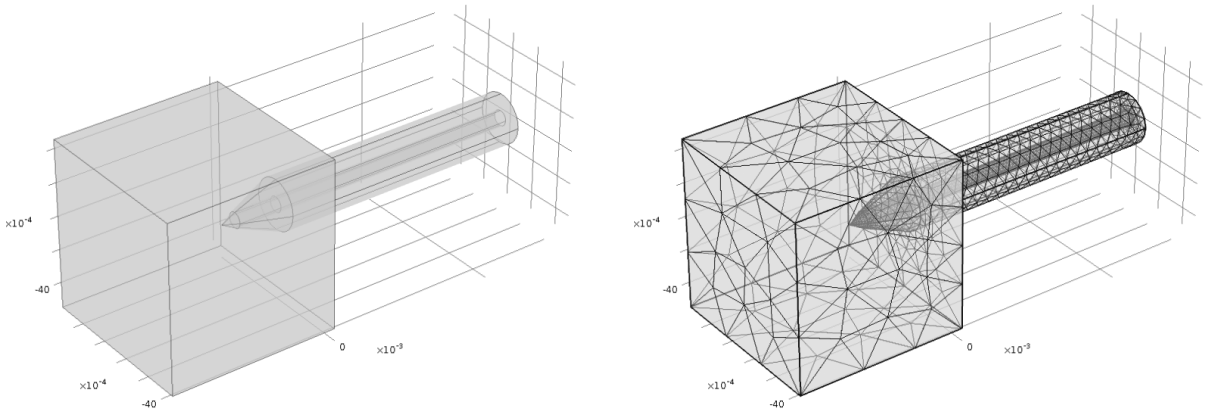

Figure 3.2: Structure and triangular mesh of three dimensional conical-type coaxial probe structure.

The mesh statistics are showed in the following table.

Table 3.2 Mesh statistics.

Property	Value
Tetrahedral elements	30851
Triangular elements	4464
Edge elements	596
Vertex elements	32

The results computed by Comsol Multiphysic software are illustrated in Figures. 3.4 - 3.9 for different materials at the frequency of 1GHz and the temperature of 20 °C.

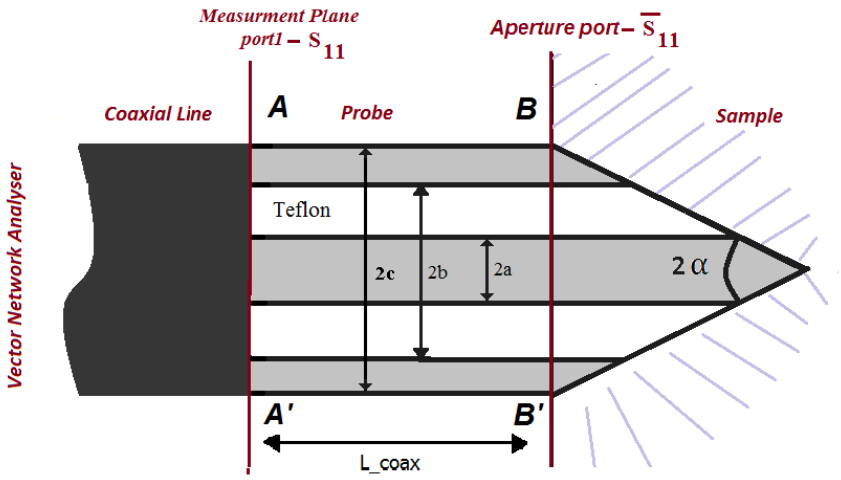

Figure 3.3: Geometry of conical-type coaxial probe structure.

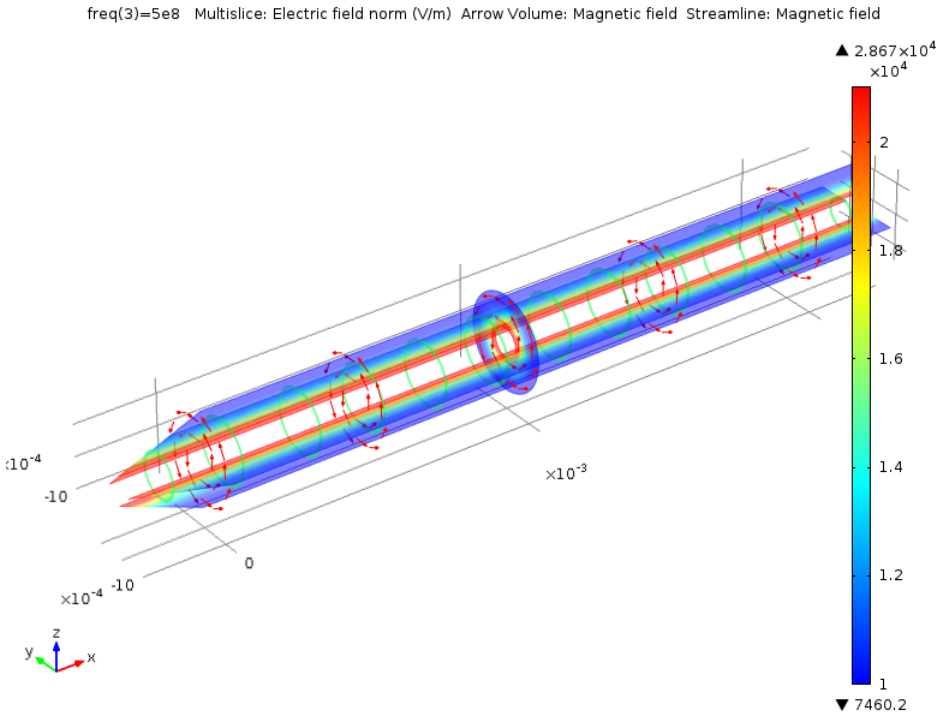

Figure 3.4: Electric field [V/m] (surface) and magnetic field [A/m](arrows) inside the coaxial cable for the state of no reflection at aperture(scattering boundary condition at the aperture).

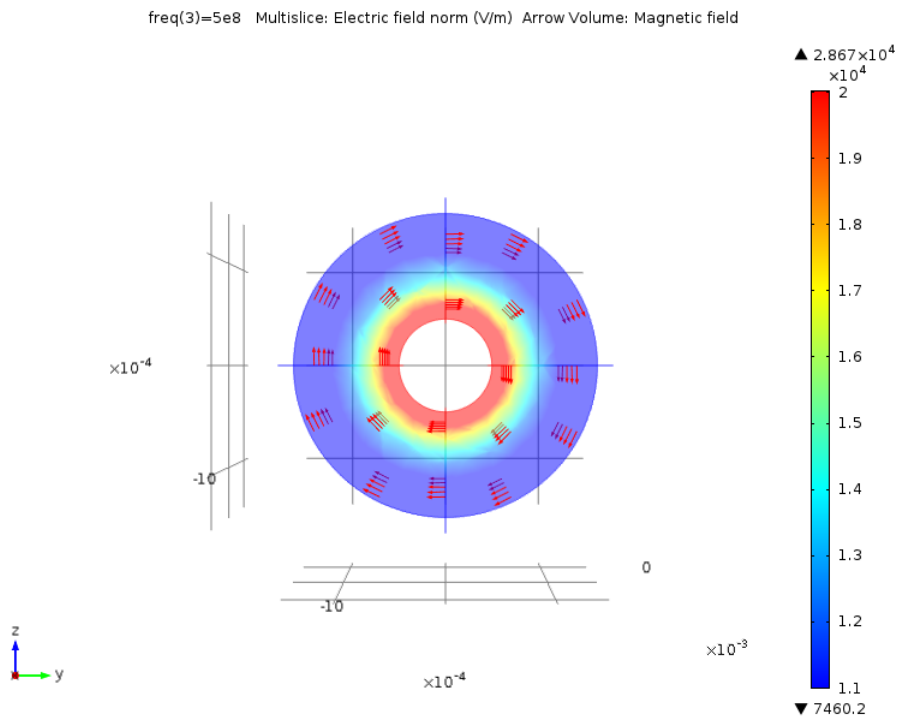

Figure 3.5: Electric field [V/m] (surface) and magnetic field [A/m](arrows) inside the conical coaxial probe for the state of no reflection at aperture (scattering boundary condition at the aperture) for z=125 [mm].

Scattering parameters (or reflection coefficient) are complex-valued, frequency dependent matrices describing the transmission and reflection coefficients of electromagnetic waves at different ports of devices. They originate from transmission-line theory and are defined in terms of transmitted and reflected electric field. To convert an electric field pattern on a port to a scalar complex number corresponding to an eigenmode expansion of the electromagnetic fields on the ports needs to be performed. The scattering parameters are given by

$$S_{11} = \frac{\iint_{port1}(E_c - E_1)E_1^* ds_1}{\iint_{port1}(E_c \cdot E_1^*)ds_1} \tag{3.15}$$

where the computed electric field E_c on the port consists of the excitation and the reflected field and E_1 is electric field at aperture port.

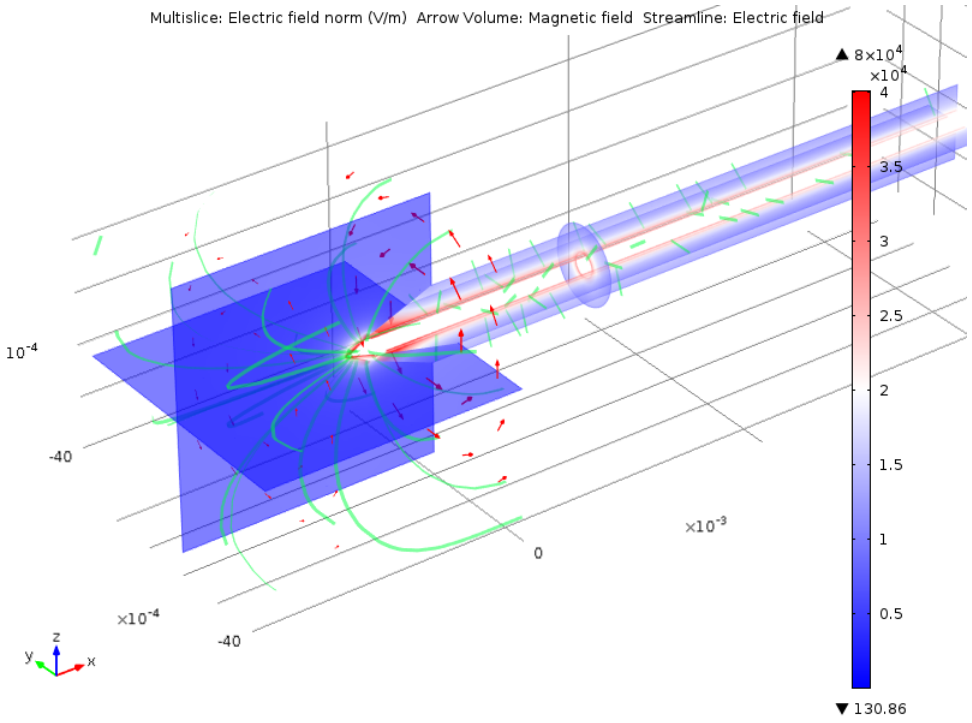

Figure 3.6: Electric field [V/m] (surface) and magnetic field [A/m](arrows) of conical $\alpha = 30\,^\circ$ coaxial probe immersed in water with $\varepsilon_r' = 79$ and $\varepsilon_r'' = 11.5$.

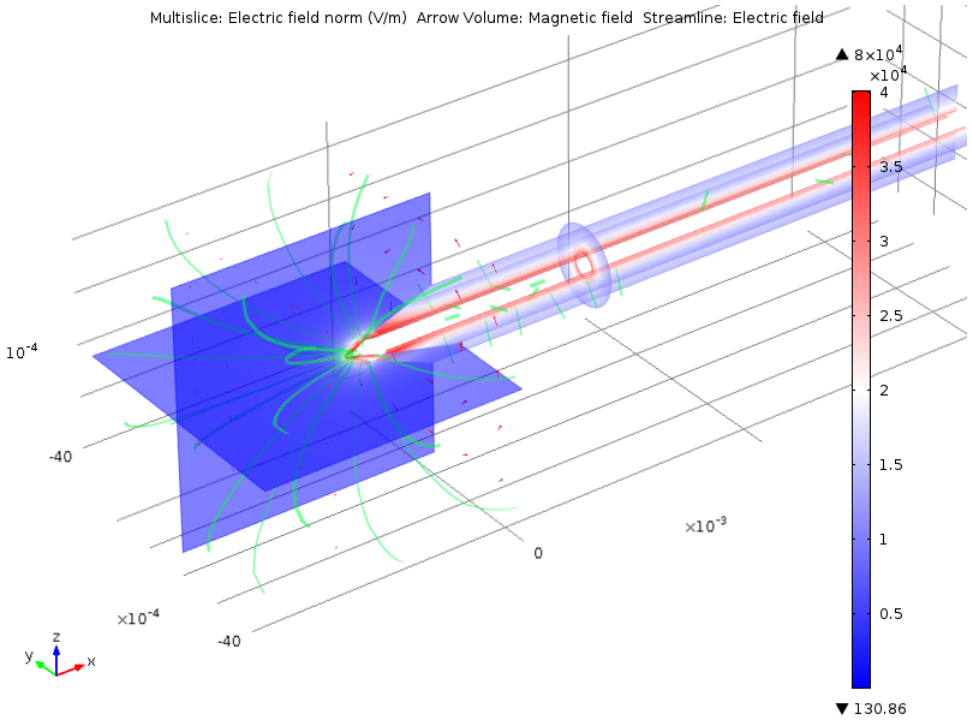

Figure 3.7: Electric field [V/m] (surface) and magnetic field [A/m](arrows) of conical $\alpha = 30\,^\circ$ coaxial probe immersed in methanol with $\varepsilon_r' = 32$ and $\varepsilon_r'' = 13$.

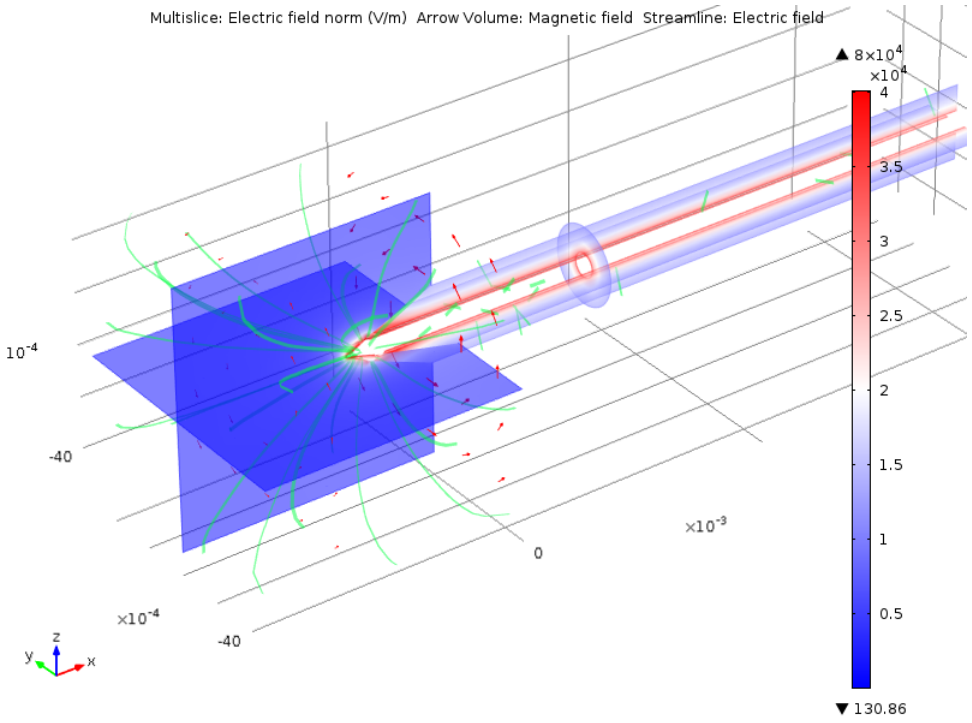

Figure 3.8: Electric field [V/m] (surface) and magnetic field [A/m](arrows) of conical $\alpha = 30\,^\circ$ coaxial probe immersed in butanol with $\varepsilon_r' = 18$ and $\varepsilon_r'' = 6.5$.

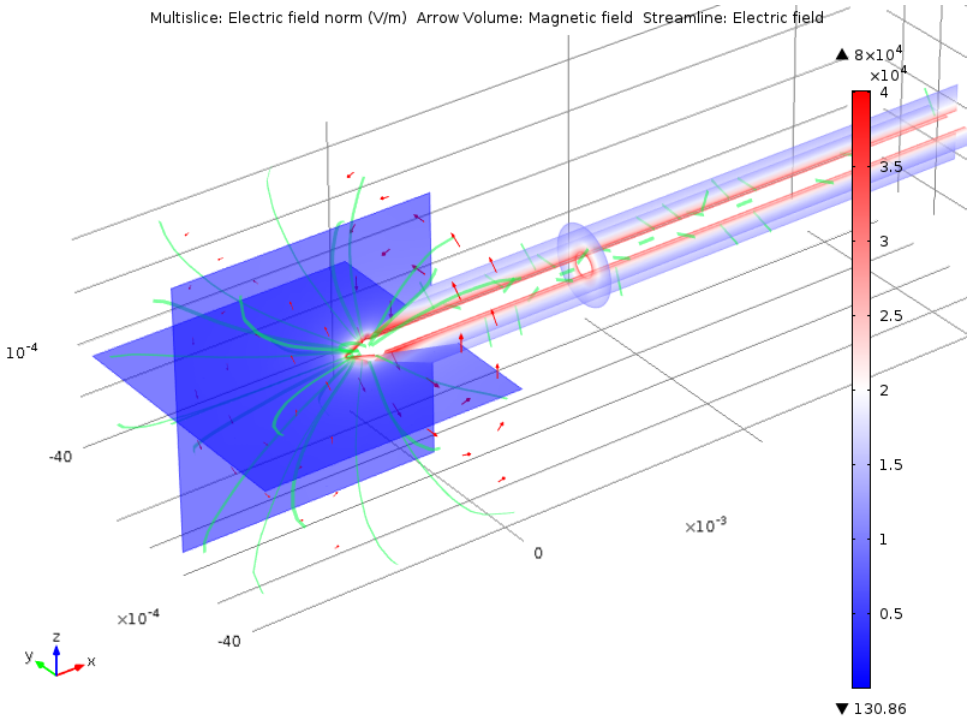

Figure 3.9: Electric field [V/m] (surface) and magnetic field [A/m](arrows) of conical $\alpha = 30\,^\circ$ coaxial probe immersed in propanol with $\varepsilon_r' = 20$ and $\varepsilon_r'' = 8$.

Figures. 3.10 - 3.13 show the measured reflection coefficient S_{11} of air, water, methanol and butanol at the temperature of 20 °C with conical type open ended coaxial probe by using Comsol Multiphysic software.

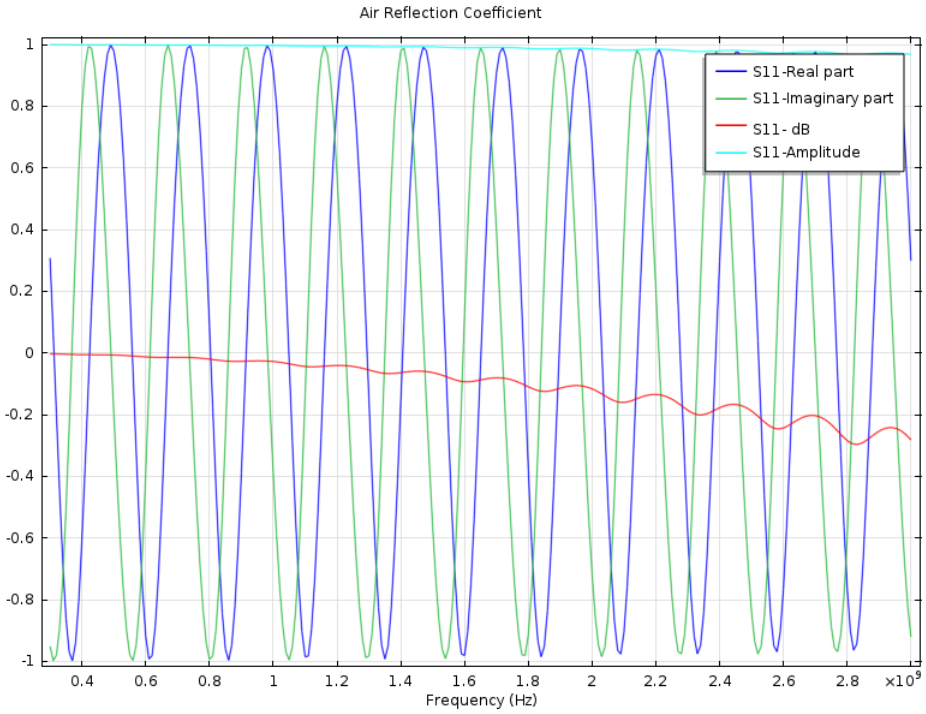

Figure 3.10: Reflection coefficient for air at measurement port (S_{11}).

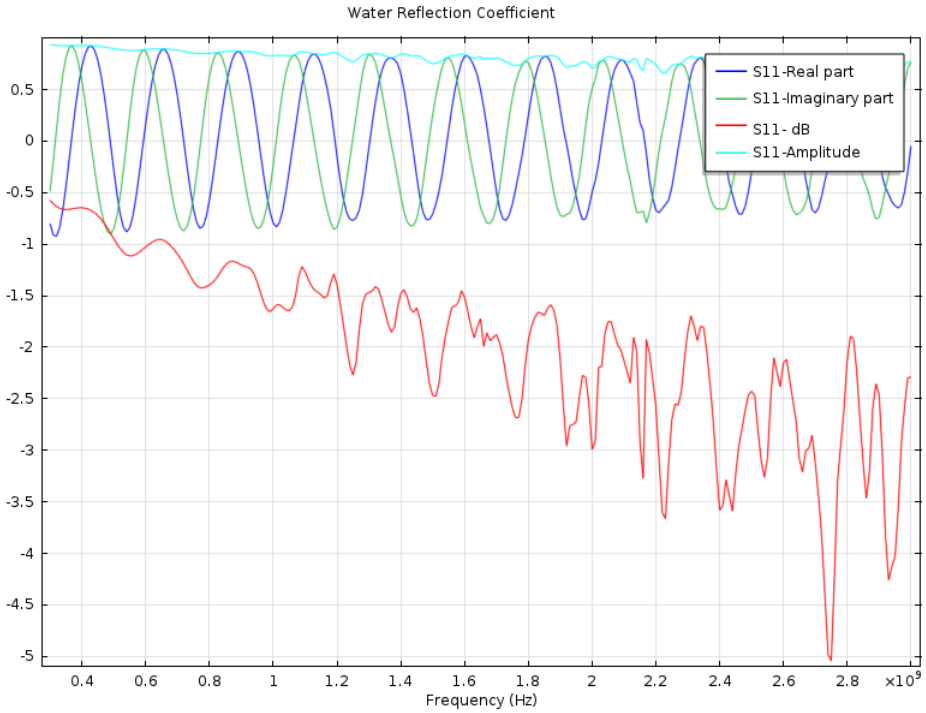

Figure 3.11: Reflection coefficient for water at measurement port (S_{11}).

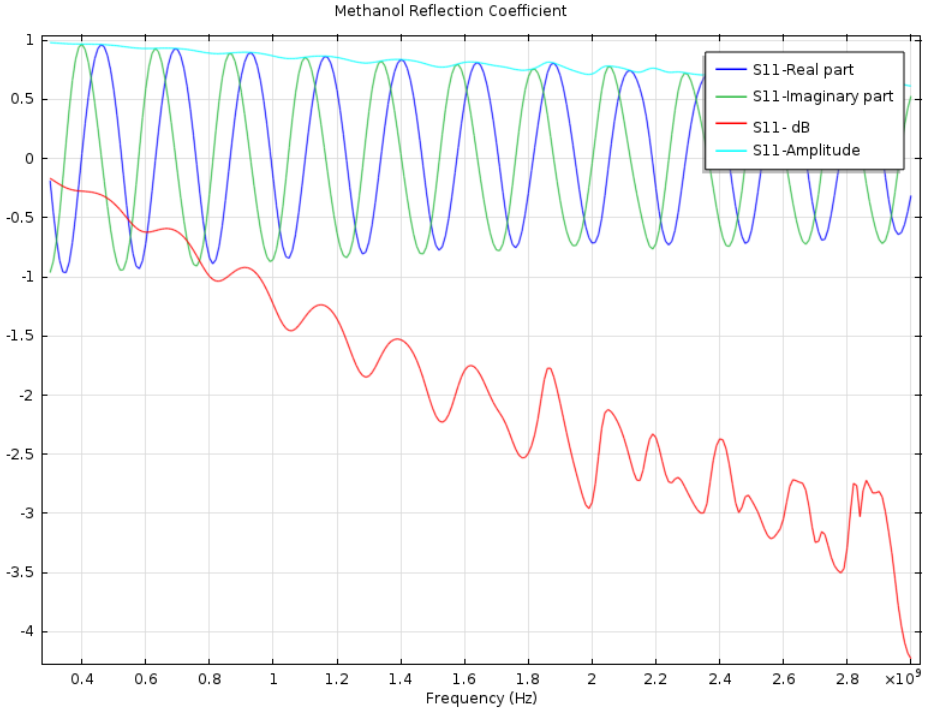

Figure 3.12: Reflection coefficient for methanol at measurement port (S_{11}).

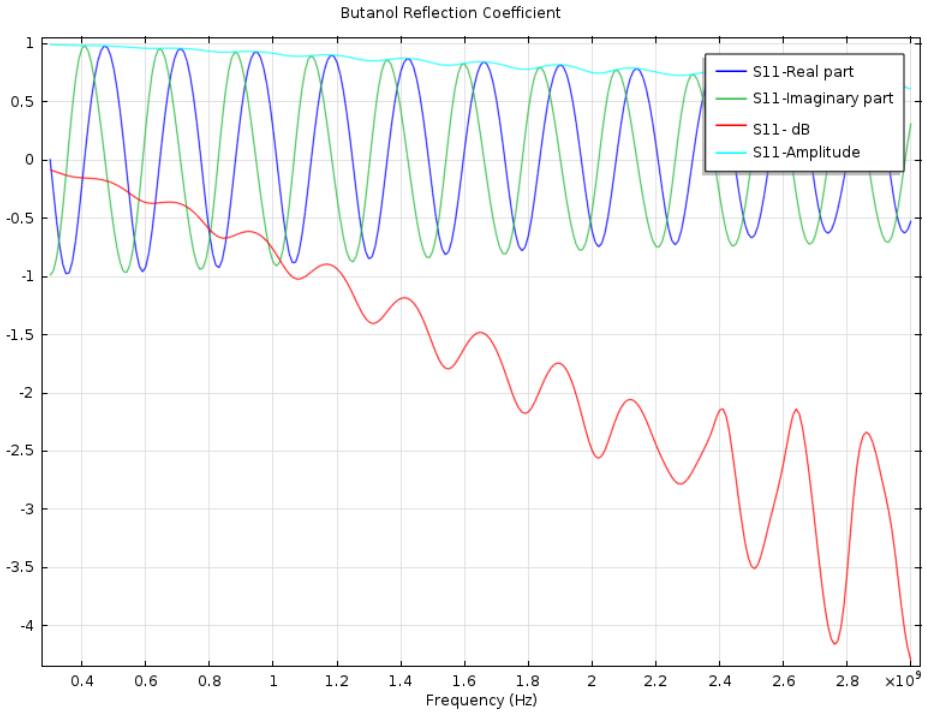

Figure 3.13: Reflection coefficient for butanol at measurement port (S_{11}).

Since this model requires a reflection coefficient value referred at the $A - A'$ plane, the phase difference between the $B - B'$ and $A - A'$ planes must be considered (See Figure 3.1 for the definition of these two planes.). The reflection coefficients relative to these two planes are related in this way:

$$\overline{S_{11}} = S_{11} e^{2jkL_{coax}}; \tag{3.16}$$

$$k = \frac{2\pi}{\lambda}, \tag{3.17}$$

where $\overline{S_{11}}$ is reflection coefficient in plan $A - A'$.

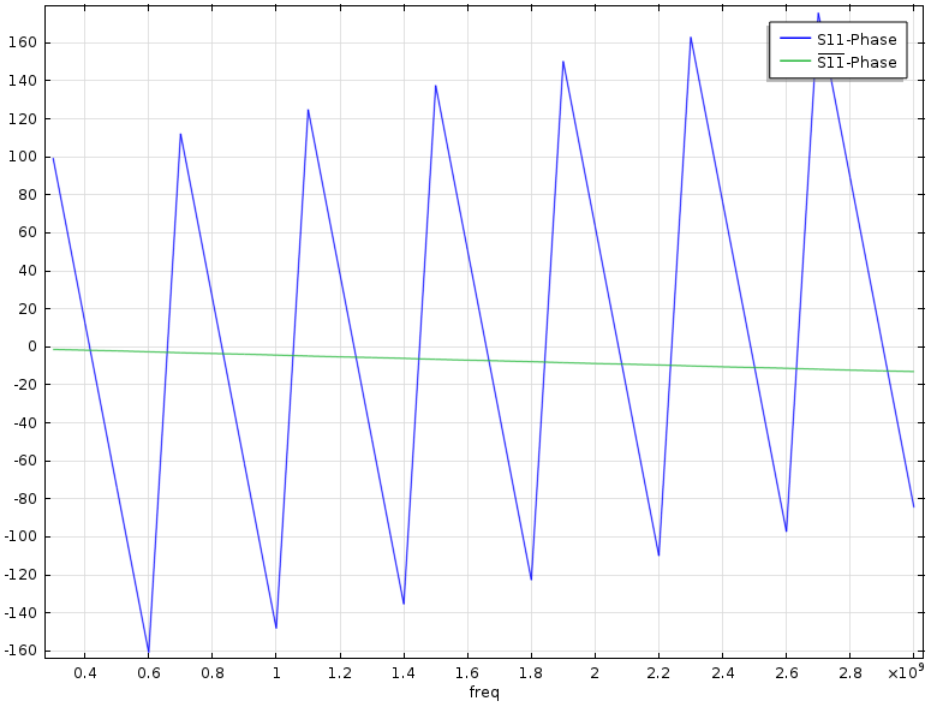

Figure 3.14: Phase of S_{11} and $\overline{S_{11}}$ of open ended conical $\alpha = 30\,^\circ$ coaxial probe in air [deg].

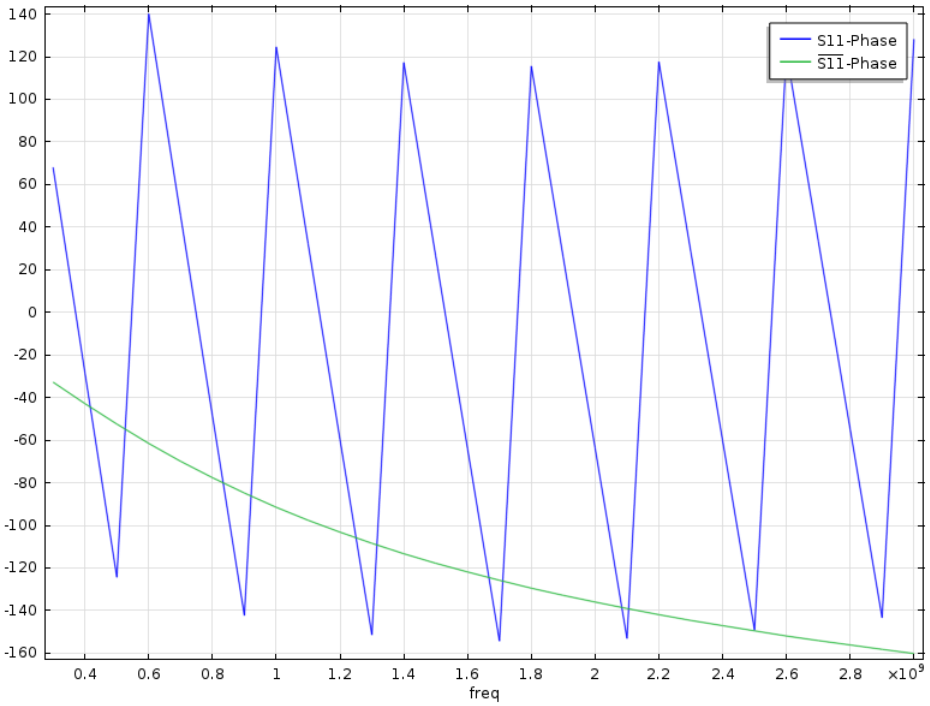

Figure 3.15: Phase of S_{11} and $\overline{S_{11}}$ of conical $\alpha = 30\,^\circ$ coaxial probe immersed in water [deg].

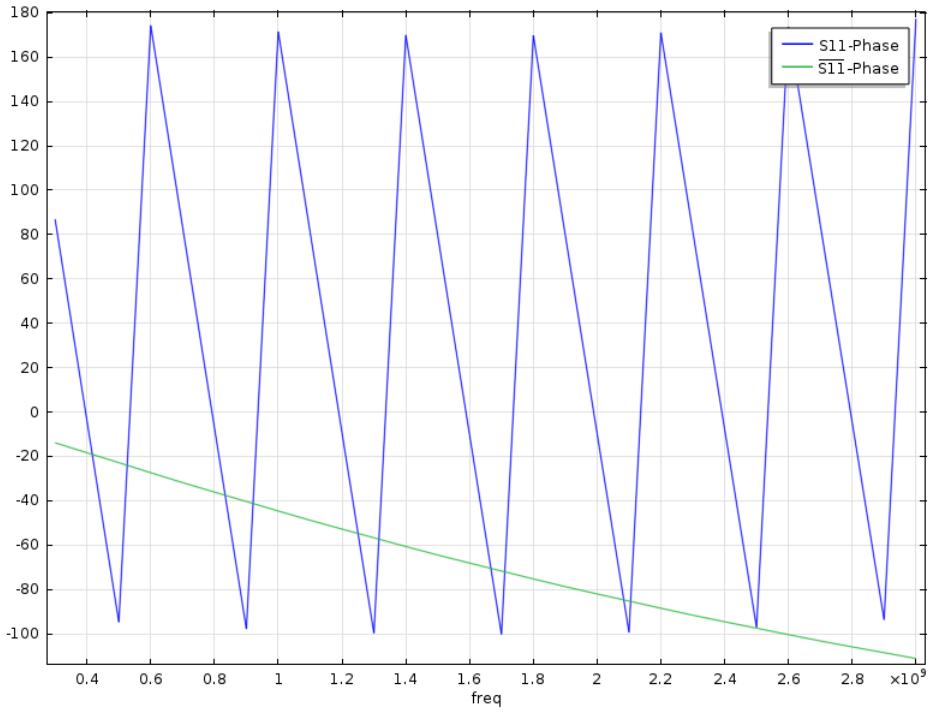

Figure 3.16: Phase of S_{11} and $\overline{S_{11}}$ of conical $\alpha = 30\,^\circ$ coaxial probe immersed in methanol [deg].

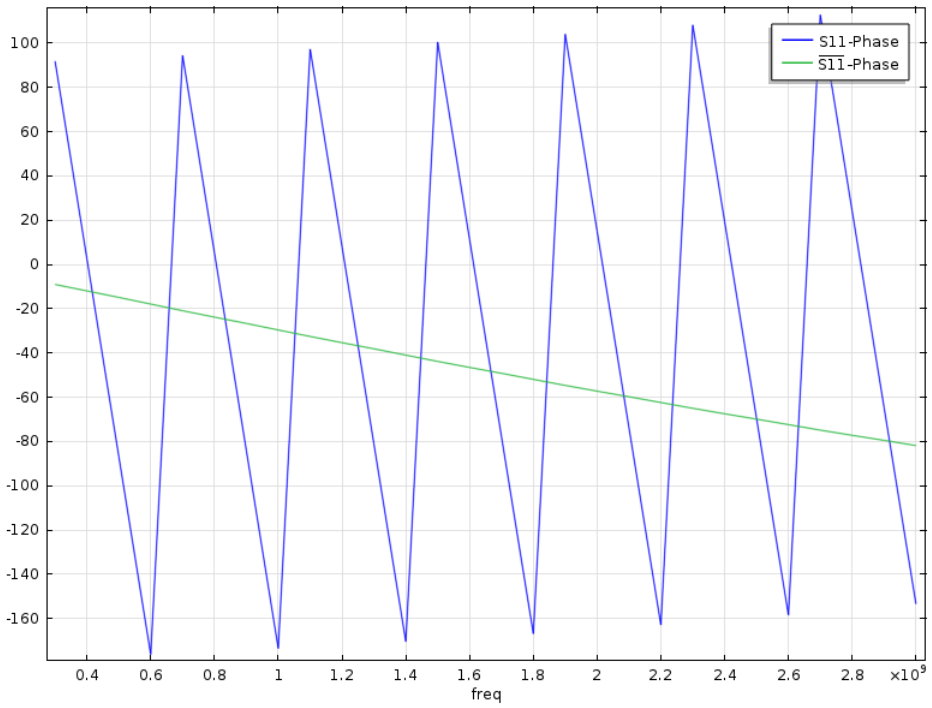

Figure 3.17: Phase of S_{11} and $\overline{S_{11}}$ of conical $\alpha = 30\,^\circ$ coaxial probe immersed in butanol [deg].

Table 3.3, shows the amplitude and the phase of the reflection coefficient at measurement port $A - A', (S_{11})$ and at aperture port $B - B', (\overline{S_{11}})$, and in Table 3.4 demonstrates admittance $Y = Y_0 \dfrac{1 - \overline{S_{11}}}{1 + \overline{S_{11}}}, Y_0 = 0.02$ for different materials under test.

Table 3.3 S_{11} and $\overline{S_{11}}$ amplitude and phase for different materials at $f = 1GHz$.

freq=1GHz	Amp S_{11}	Phase S_{11}	Amp $\overline{S_{11}}$	Phase $\overline{S_{11}}$
Air	0.999	-147.955	0.999	-4.107
Water	0.898	124.132	0.898	-92.021
Methanol	0.955	171.370	0.956	-44.782
Butanol	0.9752	-173.435	0.975	-29.588

Table 3.4 Input admittance for different materials.

freq	Admittance-Air	Admittance-Water	Admittance-Methanol	Admittance-Butanol
3.0E8	8.824E-7+2.379E-4i	1.705E-4+0.006i	4.493E-5+0.0024i	2.334E-5+0.0016i
6.0E8	3.531E-6+4.535E-4i	7.068E-4+0.012i	1.822E-4+0.0049i	9.396E-5+0.003i
9.0E8	7.931E-6+6.766E-4i	0.0017+0.0182i	4.183E-4+0.0073i	2.141E-4+0.0047i
1.2E9	1.410E-5+9.199E-4i	0.003+0.025i	7.656E-4+0.01i	3.868E-4+0.0064i
1.5E9	2.207E-5+0.0012i	0.006+0.0324i	0.0012+0.0126i	6.192E-4+0.0081i
1.8E9	3.181E-5+0.0014i	0.0093+0.0407i	0.0019+0.0153i	9.169E-4+0.0097i
2.1E9	4.3294E-5+0.0016i	0.0148+0.0497i	0.0027+0.0182i	0.0012+0.01146i
2.4E9	5.671E-5+0.0018i	0.0231+0.0595i	0.0038+0.0213i	0.0017+0.0133i
2.7E9	7.2035E-5+0.0021i	0.0359+0.0695i	0.0052+0.0246i	0.0023+0.0152i
3.0E9	8.909E-5+0.0023i	0.055+0.0773i	0.0069+0.0281i	0.003+0.0171i

In Chapter 4, the input admittance and reflection coefficients calculated in this chapter for different materials will be used for computing relative permittivity and conductivity of MUT.

CHAPTER 4

DIFFERENT MODELS OF THE CONICAL TYPE COAXIAL PROBE

In this chapter, a comparative study of three different conical-type open-ended coaxial probe equivalent circuit models which relate the coaxial line end impedance to the complex permittivity of the material under test is presented. The three conical-type open-ended coaxial probe models studied are:

1. Capacitive model;
2. Antenna model;
3. Improved virtual line model.

Using simulations, these three models are investigated for the conical type coaxial probe with respect to measuring relative permittivity and conductivity. A certain number of studies for these models exist for the flat coaxial probe in the literature [24–27]; however, no studies are available in the open literature to assess these models for the conical type coaxial probes. The main goal of this chapter is to find a robust and accurate model for the conical type coaxial probe in order to accurately calculate the dielectric properties of the various materials by using the reflection coefficient that was calculated in the previous chapter.

4.1 Capacitive Model

The equivalent circuit for this model consists of three capacitors connected in parallel, which is presented in Figure 4.1. The geometrical specifications of the structure of probe are shown in Table 4.1. The model is described in details in references [11, 28, 29]. When a dielectric sample with complex relative permittivity is connected to the probe, the reflection coefficient $\overline{S_{11}}$ at the aperture of the open-ended probe is obtained by considering the complex admittance of the equivalent circuit, the reflection coefficient is given by:

$$\overline{S_{11}} = \frac{1 - j\omega Z_0(C_{cone} + C_f + \varepsilon_r C_0)}{1 + j\omega Z_0(C_{cone} + C_f + \varepsilon_r C_0)}, \tag{4.1}$$

where C_{cone} is the capacitance of the Teflon-filled conical coaxial probe, C_f and C_0 are the capacitance of the fringe field at aperture port, ω is the angular frequency ($2\pi f$) and Z_0 is the characteristic impedance of the coaxial line. The complex relative permittivity (ε_r) is

given by:

$$\varepsilon_r = \frac{1 - \overline{S_{11}}}{j\omega Z_0 C_0 (1 + \overline{S_{11}})} - \frac{C_{cone} + C_f}{C_0}. \tag{4.2}$$

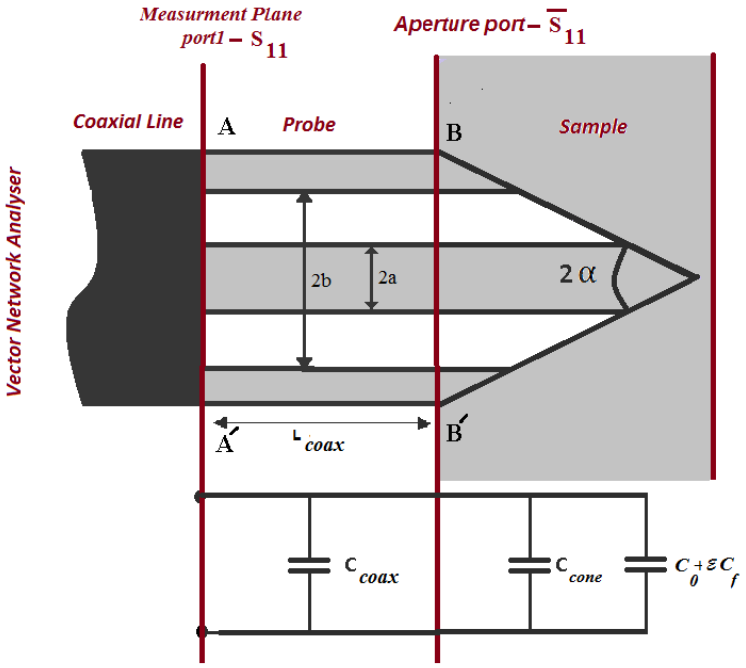

Figure 4.1: Conical-type coaxial probe geometry and equivalent circuit.

Table 4.1 The geometrical specifications of the structure.

Name	Expression	Description
a	0.455 [mm]	Coax inner radius
b	1.49 [mm]	Coax outer radius
L_{coax}	250 [mm]	Length of conical coax probe
f	300 [MHz]- 3 [GHz]	Frequency
α	30 °	Cone Angle

The analytical computation of C_{cone} part is complicated due to the different geometrical parameters of the structure. For this reason, we will use an approximate alternative method to do the calculation of C_{cone}. The first technique being used here is comparing the reflection coefficient at port $B - B'$ of two different probe types, flat and conical coaxial probes. The difference between the admittance of both of the probes is related to the conical part of the conical coaxial probe capacitance. The second method is dividing the aperture into many

thin layers and each layer can be approximated by a constant radius which is an elegant way to calculate C_{cone} accurately. The results of both methods are in good agreement as shown in Figure 4.2. In Table 4.2 the results of different calculated capacities of the probe and fringe fields (air) at different frequencies are presented.

Table 4.2 Capacitance of the cone part of the probe C_{cone} and fringing field $C_{net} = C_f + C_0$ [F].

freq	C_{cone}	$C_{net} = C_f + C_0$
300000000	9.96E-14	1.96E-14
600000000	9.96E-14	1.97E-14
900000000	9.96E-14	1.99E-14
1200000000	9.96E-14	2.01E-14
1500000000	9.96E-14	2.044E-14
1800000000	9.96E-14	2.07E-14
2100000000	9.96E-14	2.10E-14
2.40E+09	9.96E-14	2.13E-14
2.70E+09	9.96E-14	2.15E-14
3.00E+09	9.96E-14	2.17E-14

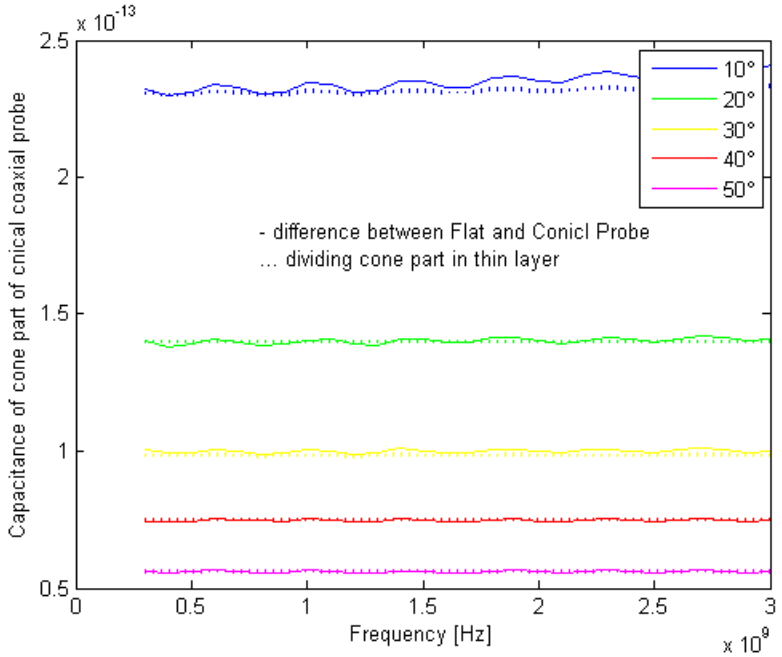

Figure 4.2: Capacitance of cone part for different angle of conical coaxial probe.

In Figure 4.3 C_0 and C_f are illustrated separately. Numerical methods are used to calculate values of the total fringing capacitance C_{net} for both Air and Water. From this data, the

values of C_0 and C_f are obtained by solving the simultaneous linear equation $C_{net} = C_f + \varepsilon C_0$. As we can see the amount of C_f is small in comparison to C_0 and it is related to the frequency.

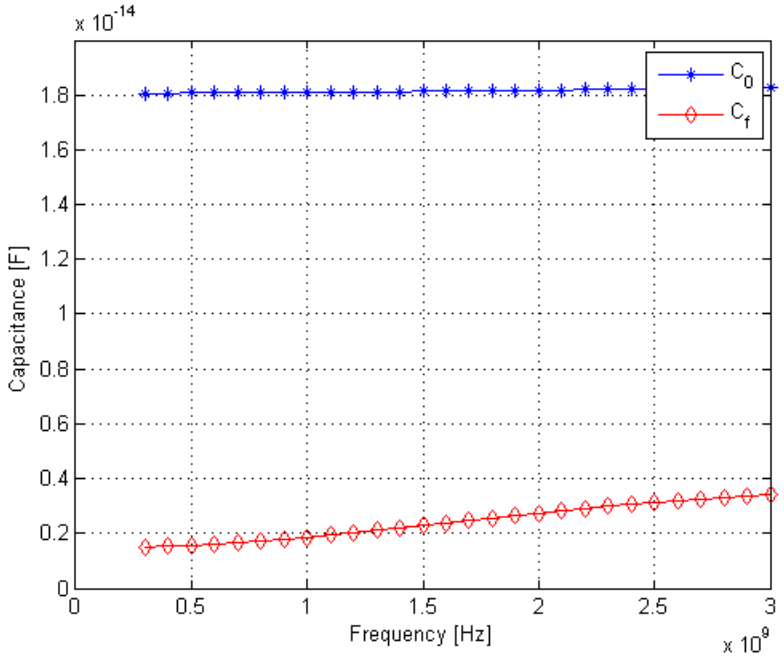

Figure 4.3: Capacitances of the fringing field - Conical coaxial probe ($\alpha = 30\,^\circ$) [F].

After the calculation of these parameters, we are able to calculate the complex dielectric permittivity of a medium using equation 4.2, as the results are shown in Figure 4.4 and Figure 4.5.

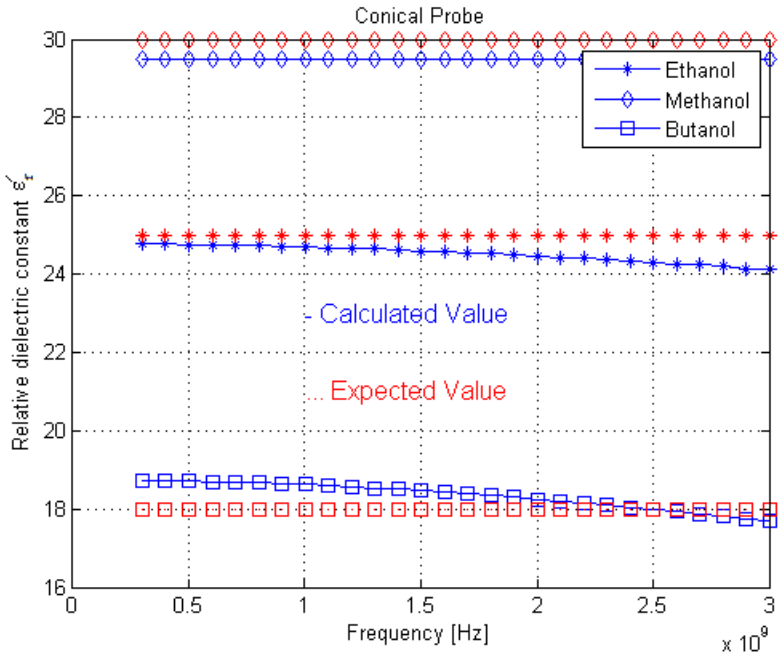

Figure 4.4: Measured relative dielectric constant for open ended conical coaxial probe ($\alpha = 30\,^\circ$) versus frequency.

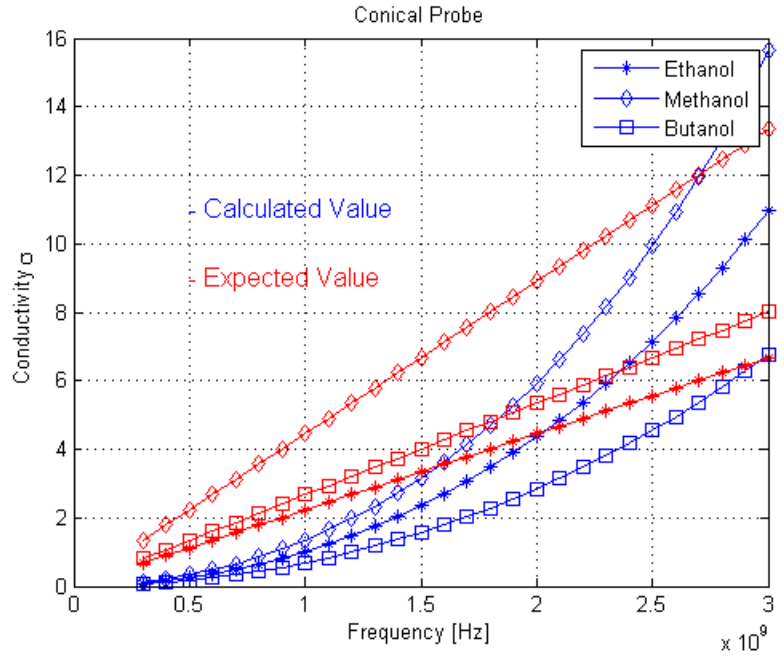

Figure 4.5: Conductivity for open ended conical coaxial probe ($\alpha = 30\,^\circ$) versus frequency [S/m].

From above results, we can see that the Capacitive Model is a good approximation for relative permittivities, but it is not so accurate for conductivities. Expected results are related to

values of relative permittivity and conductivity we used in Comsol simulations (these values can be found in the references).

4.2 Antenna Model

In the antenna model, the cone part of the conical probe is modelled by C_{cone}, while the material under test (MUT) is modelled by a capacitor $C_{net} = C_f + \varepsilon C_0$ and a conductor G connected in parallel to the capacitor for modelling the radiation in MUT [30, 31]. The 2-dimensional electromagnetic structure of the conical-type open-ended coaxial probe shown in Figure 4.6 is considered. The geometrical specification of the structure are presented in Table 4.1.

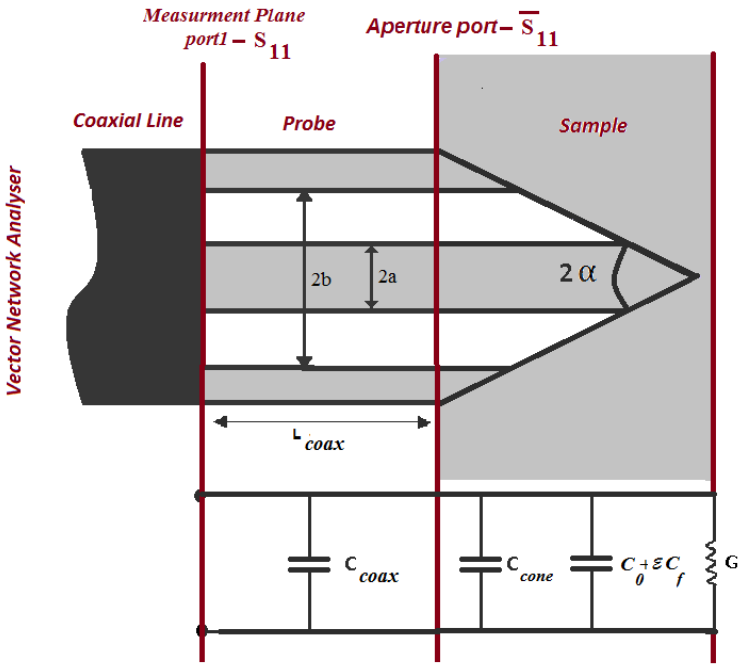

Figure 4.6: Conical-type coaxial probe geometry and equivalent circuit.

The normalized admittance of this equivalent circuit at the aperture port is given by:

$$\frac{Y}{Y_0} = j\omega C_{cone} Z_0 + j\omega C_{net} Z_0(\omega, \varepsilon_0) + Z_0 G(\omega, \varepsilon_0). \tag{4.3}$$

For coaxial line whose dimensions are small compared to a wavelength, C_f and C_{cone} are frequency independent, while C_0 and G are dependent on frequency. For a coaxial probe

immersed in a lossy medium it has been shown in [32–34] that:

$$Y(\omega, \varepsilon) = \sqrt{\varepsilon} Y(\sqrt{\varepsilon}\omega, \varepsilon_0). \tag{4.4}$$

Hence, equation 4.3 may be written:

$$\frac{Y}{Y_0} = j\omega C_{cone} Z_0 + j\omega C_f Z_0 + j\omega\varepsilon C_0 Z_0 + Z_0 G \varepsilon^{5/2}. \tag{4.5}$$

These unknown capacitances and conductances are estimated accurately by using two material with known properties (air and water). The results at different frequencies are shown in Table 4.3 for conical and flat probes.

Table 4.3 Free space radiation conductance (G), the fringing field capacitance (C_{net}) and (C_{cone}).

Frequency	Conical Probe		Flat Probe	
	G [s]	$C_{net} + C_{cone}$ [F]	G [s]	C_{net} [F]
300000000	3.25E-08	1.19E-13	9.15E-07	1.96E-14
600000000	1.44E-07	1.19E-13	4.10E-06	1.97E-14
900000000	3.89E-07	1.20E-13	1.13E-05	1.99E-14
1200000000	9.08E-07	1.20E-13	2.73E-05	2.01E-14
1500000000	2.11E-06	1.20E-13	6.71E-05	2.04E-14
1800000000	5.44E-06	1.21E-13	1.93E-04	2.07E-14
2100000000	1.88E-05	1.21E-13	8.69E-04	2.10E-14
2.40E+09	1.75E-04	1.22E-13	0.054175266	2.13E-14
2.70E+09	4.45E-04	1.22E-13	0.002792891	2.15E-14
3.00E+09	4.80E-05	1.22E-13	7.37E-04	2.17E-14

Figures 4.7 and 4.8 show relative permittivity and conductivity for three different materials (Ethanol, Methanol, and Butanol) obtained with a conical type open-ended coaxial probe. These permittivities are calculated from the reflection coefficient measured in Chapter 3. The use of such model is a good approximation for large range of permittivities at radio and microwave frequencies.

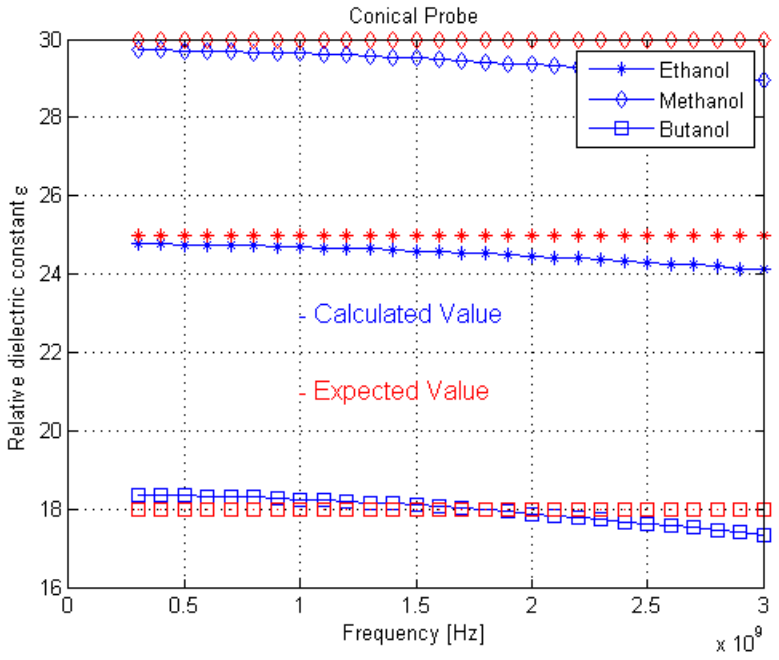

Figure 4.7: Relative dielectric constant for open ended conical coaxial probe (cone angle 30 degree) versus frequency.

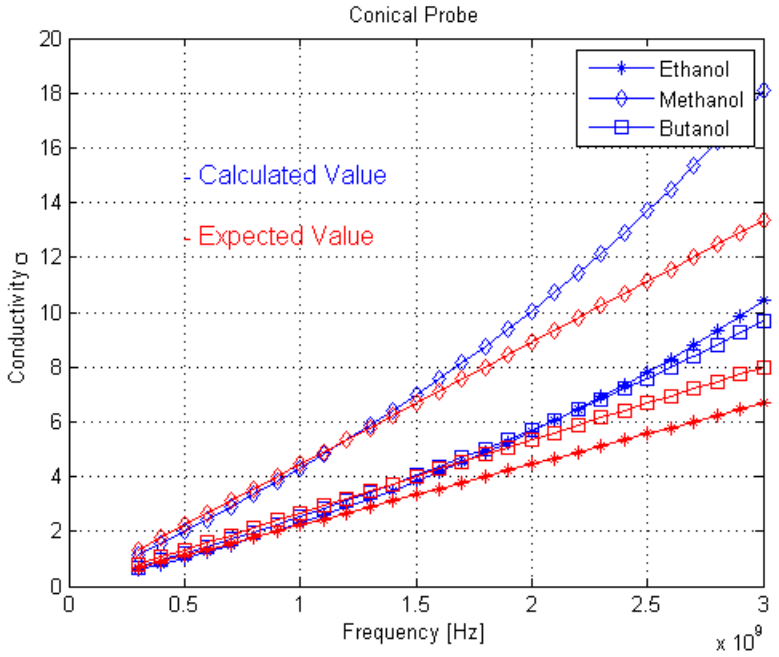

Figure 4.8: Conductivity for open ended conical coaxial probe ($\alpha = 30\,^{\circ}$) versus frequency [S/m].

The results show that open-ended conical coaxial probes can be successfully used especially at low frequencies with the advantage of increased accuracy and sensitivity in comparison

to the capacitive model. Moreover,the results are same in specific range of temperature ($20\,^{\circ}\mathrm{C} - 30\,^{\circ}\mathrm{C}$). Hence, it is less affected by the unavoidable temperature variation when compared to standard flat-plan open-circuit coaxial-probe.

4.3 Improved virtual line model

This model was studied in references [30, 35] for a flat coaxial probe. This method consists of modelling the dielectric medium by a improved virtual open ended transmission line of which has the same dimensions as the physical line, this is shown in Figure 4.9. According to the conventional transmission-line theory the admittance at $B - B'$ plane is given by:

$$Y_{BB'} = Y_{0BB'} \frac{Y_L + jY_{0BB'} \tan(\beta_t D)}{Y_{0BB'} + jY_L \tan(\beta_t D)}, \tag{4.6}$$

for open ended probe, we have:

$$Y_{BB'} = jY_{0BB'} \tan(\beta_t D); \tag{4.7}$$

$$Y_{0BB'} = \frac{\sqrt{\varepsilon_t}}{60 \ln(\frac{R_{coax}}{r_{coax}})}, \tag{4.8}$$

where D is the virtual transmission line length, $Y_{0BB'}$ is the characteristic admittance of the virtual transmission line, ε_t is relative permittivity of MUT, and ε_r is relative permittivity of Teflon inside the conical coaxial probe. In addition, the refereed characteristic admittance at the input of the aperture of the conical probe is as follows:

$$Y_{BB'} = Y_{0AA'} \frac{1 - \Gamma_{AA'} e^{2j\beta_P L_{coax}}}{1 + \Gamma_{AA'} e^{2j\beta_P L_{coax}}}; \tag{4.9}$$

$$Y_{0AA'} = \frac{\sqrt{\varepsilon_r}}{60 \ln(\frac{R_{coax}}{r_{coax}})}. \tag{4.10}$$

The admittance is defined in presence of the MUT (Figure 4.9) is:

$$Y = Y_{0AA'} \frac{1 - \Gamma_{AA'} e^{2j\beta_P L_{coax}}}{1 + \Gamma_{AA'} e^{2j\beta_P L_{coax}}} - jY_{0BB'} \tan(\beta_t D) \tag{4.11}$$

Therefore, the relation between a measured reflection coefficient and the complex permittivity can be formulated into the following equations as:

$$y = \sqrt{\varepsilon_r}\frac{1-\Gamma_{AA'}e^{2j\beta_P L_{coax}}}{1+\Gamma_{AA'}e^{2j\beta_P L_{coax}}} - j\sqrt{\varepsilon_t}\tan(\beta_t D); \tag{4.12}$$

$$Y = \frac{y}{60\ln(\frac{R_{coax}}{r_{coax}})}; \tag{4.13}$$

$$D = \frac{1}{\beta_t}tan^{-1}(\frac{-j}{\sqrt{\varepsilon_t}}(\frac{1-\Gamma_{AA'}e^{2j\beta_P L_{coax}}}{1+\Gamma_{AA'}e^{2j\beta_P L_{coax}}}\sqrt{\varepsilon_r} - y)); \tag{4.14}$$

$$\varepsilon_t = ((\frac{1-\Gamma_{AA'}e^{2j\beta_P L_{coax}}}{1+\Gamma_{AA'}e^{2j\beta_P L_{coax}}}\sqrt{\varepsilon_r} - y)\cot(\beta_t D))^2. \tag{4.15}$$

Two unknown parameters, y and D are calculated accurately by using two materials with known properties (air and water).

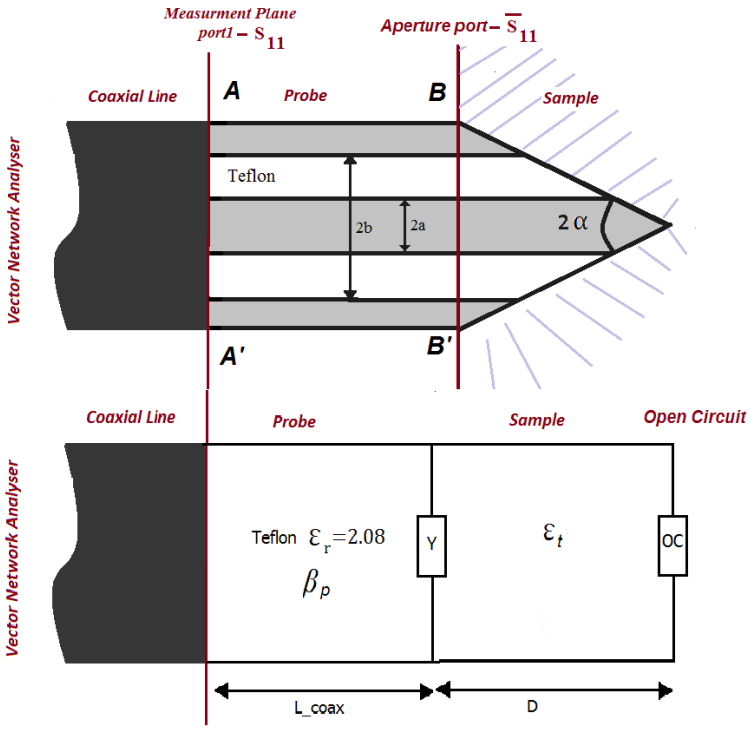

Figure 4.9: Geometry and equivalent improved virtual transmission-line model of an open-ended conical type coaxial probe.

Figures 4.10 and 4.11 show the two constants y and D related to virtual line part and Figures 4.12 and 4.13 show relative permittivity and conductivity for three different materials (methanol, butanol, and ethanol) at a temperature of 20 °C with conical type open ended coaxial probe. These permittivities are calculated from the reflection coefficient measured

at measurement port (plane $A - A'$) in Figure. 4.9. The use of such model is a good approximation for large band of permittivities at radio and microwave frequencies.

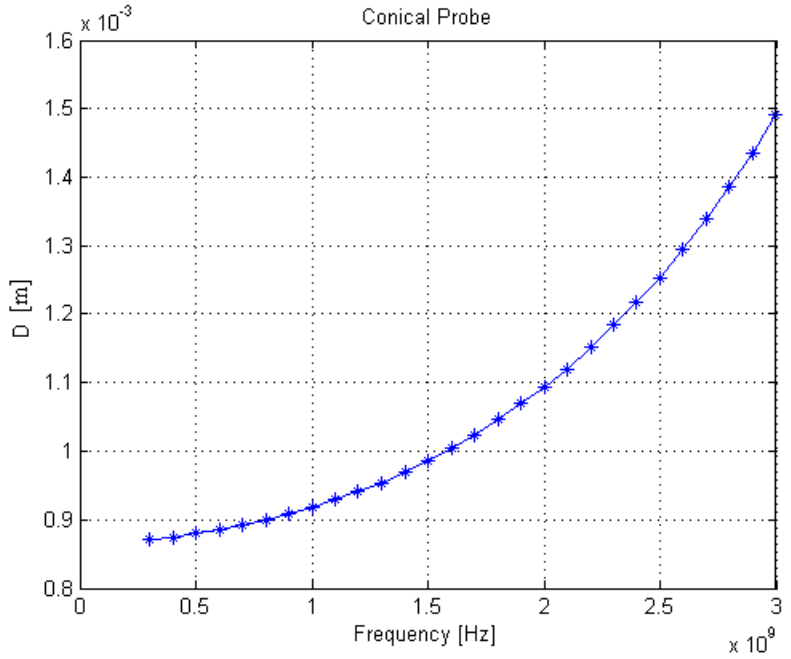

Figure 4.10: Improved virtual line model's line (D) for conical coaxial probe [m].

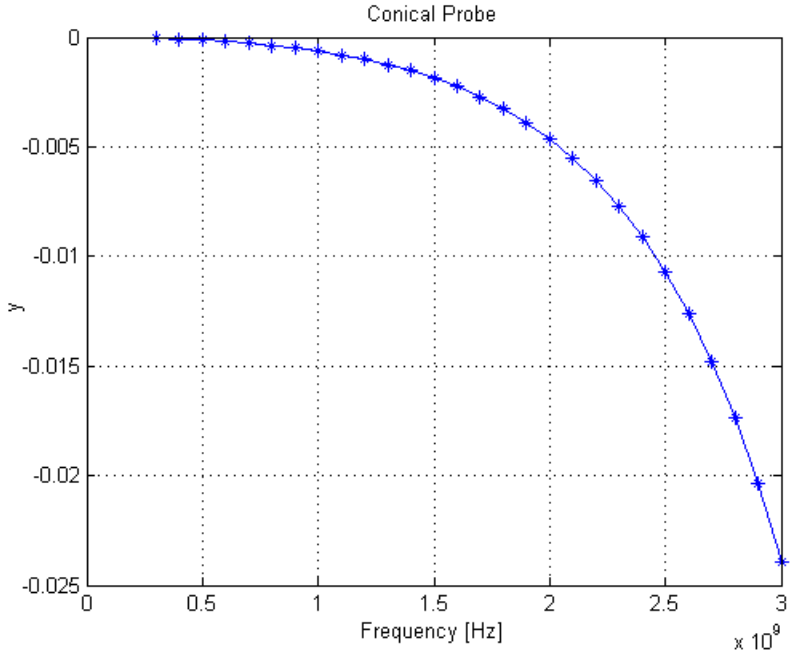

Figure 4.11: Improved virtual line model's y for conical coaxial probe.

After the calculation of these parameters, we are able to determine the complex dielectric

permittivity of a medium using equation 4.15.

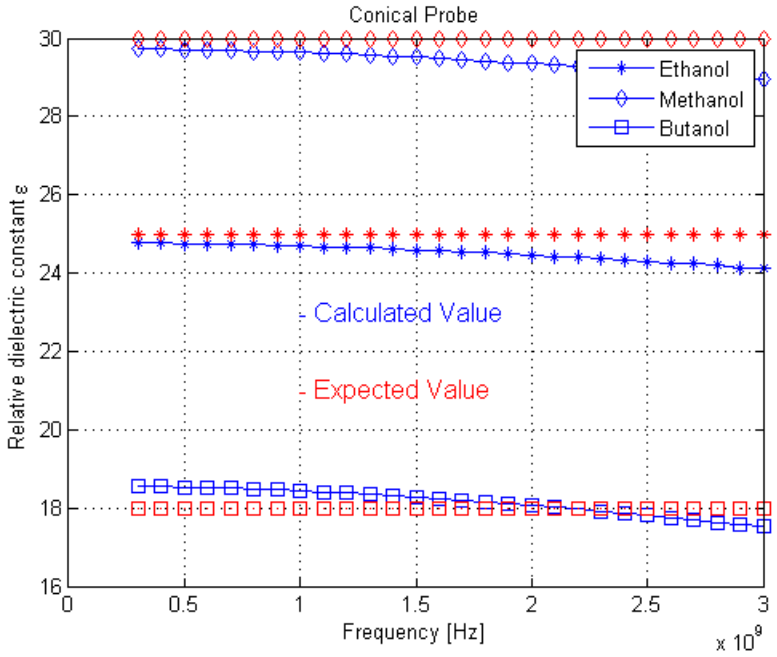

Figure 4.12: Relative dielectric constant for open ended conical coaxial probe ($\alpha = 30\,^{\circ}$) versus frequency.

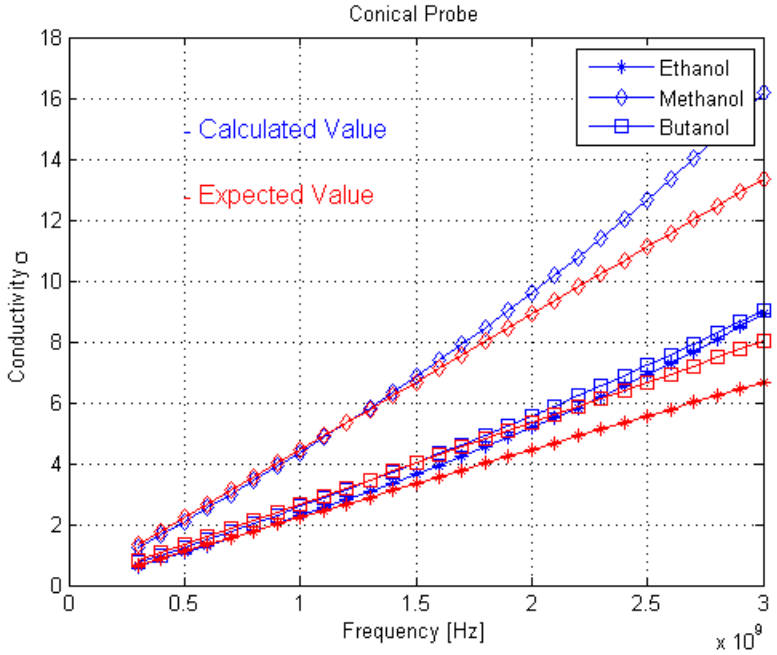

Figure 4.13: Conductivity for open ended conical coaxial probe ($\alpha = 30\,^{\circ}$) versus frequency [S/m].

Based on our study of three models, and for open ended cone probe, we can state that the results that are obtained by the improved virtual line model and the antenna model are more accurate in comparison to the capacitance model when compared to some reference results [17, 18, 36, 37]. It is worth to mention that other studies had showed the improved virtual line model is accurate for the flat probe also [30].

The obtained results by antenna model for conductivity are accurate while those obtained for relative permittivity are acceptable but the capacitive model does not give accurate results for low frequencies, especially for conductivity. It can be concluded that the improved virtual line model is more accurate in comparison with the two other models.

In Chapter 5, the simulation results provided in this chapter are compared to experimental results.

CHAPTER 5

EXPERIMENTAL MEASUREMENT RESULTS OF DIELECTRIC PROPERTIES OF MATERIAL

In this chapter of the thesis, the experiments where a conical type open-ended coaxial probe was used will be presented.

5.1 The measurement procedure

Some of the experimental setup that was used during the research is shown in Figure 5.1. It consists of three conical coaxial probes with different ending angles, 0 ° (flat), 30 °, 45 °,and a 15 ° elliptical probe made by POLY-GRAMES technicians, and vector network analyzer for measuring both amplitude and phase of S_{11}. An Agilent 85033E high temperature probe kit, with the specific range of frequency 200 MHz – 20 GHz is used for comparison with the proposed probes. The frequency range of the measurements was 300 MHz – 3 GHz with 100 points. The experiment took place in the Advanced Research Centre in Microwaves and Space Electronics (POLY-GRAMES) Department of Electrical Engineering of Ecole Polytechnique of Montreal. The calibration elements were the air (open standard), the short standard, and matched load (Agilent 85033E kit). The measurement system used here to measure the dielectric properties of liquids consisted of two different parts. The first part is used to measure the reflection coefficient of the liquids with the usage of probes of different shapes. The second part aims is comparing the results obtained in chapter four of relative permittivity and conductivity with those obtained by standard Agilent probe. Consequently, the effects of cone angle of conical coaxial probe and different types of coaxial probes (Flat-Conical-Elliptical) have been studied and reported. It can be concluded that the advantages of the sharper probe are not only in its easy insertion in materials and biological tissues, but also in the accuracy and sensitivity of this probe in the low frequency range in comparison to flat-plan open-circuit coaxial probe.

5.1.1 Reflection coefficient

In this section, the reflection coefficient of water, methanol, butanol and propanol are measured experimentally by using the conical type coaxial probe. For the measurement of the reflection coefficient of liquids, it was carefully noticed that the probe should not move at all during the measurement and the position of the probe also should be the same for different

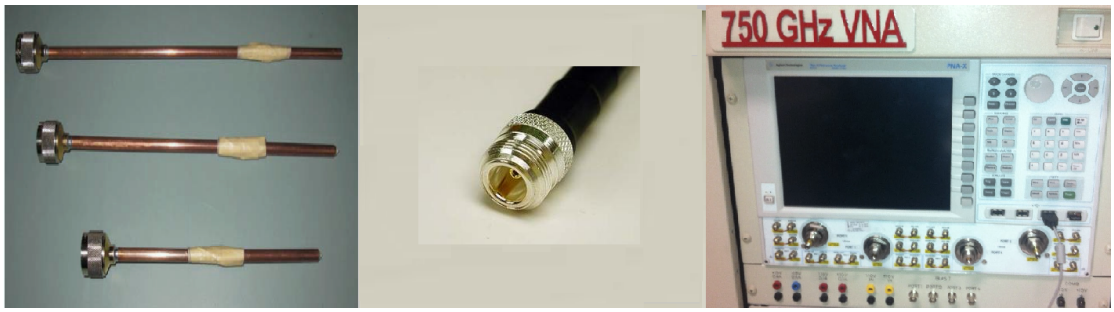

Figure 5.1: Handmade Probes and network analyzer.

liquids. There is a little difference between the experimental and numerical results which is due to a the problem in the calibration of the conical type coaxial probe. The calibration of the conical type coaxial probe/network analyzer system was done in short circuit, open circuit and matched load states. For making the matched load, the standard kit of Agilent and for short circuit an aluminium shell was used , both of these approximate solutions implies the error in the measured reflection coefficient. Figures. 5.2,5.4,5.6,5.8 show in sequence the amplitude of the reflection coefficient at aperture for water, methanol, butanol and propanol, and 5.3,5.5,5.7,5.9 show respectively the phase of the reflection coefficient at aperture for water, methanol, butanol and propanol by using conical coaxial probe.

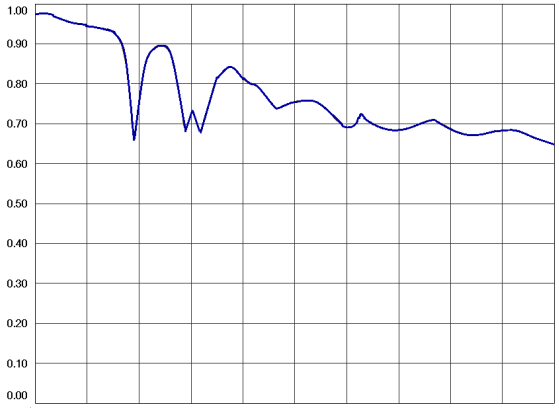

Figure 5.2: Amplitude of reflection coefficient at aperture ($\overline{S_{11}}$)-water-conical coaxial probe ($\alpha = 30\,^{\circ}$).

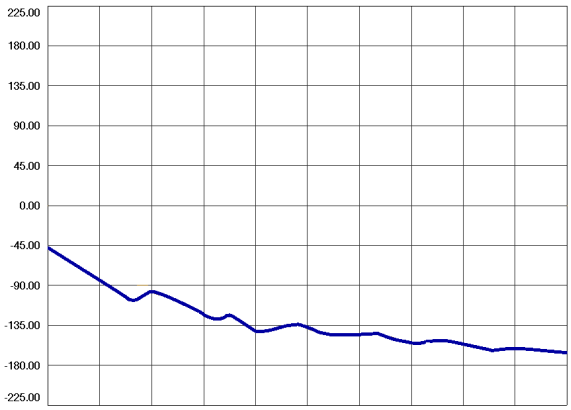

Figure 5.3: Phase of reflection coefficient at aperture ($\overline{S_{11}}$)-water-conical coaxial probe ($\alpha = 30\,^{\circ}$) [deg].

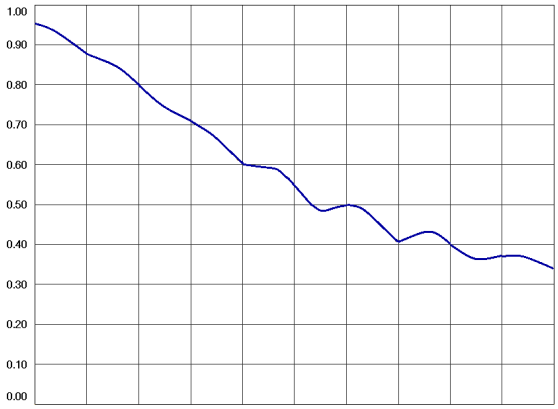

Figure 5.4: Amplitude of reflection coefficient at aperture ($\overline{S_{11}}$)-methanol-conical coaxial probe ($\alpha = 30\,^{\circ}$).

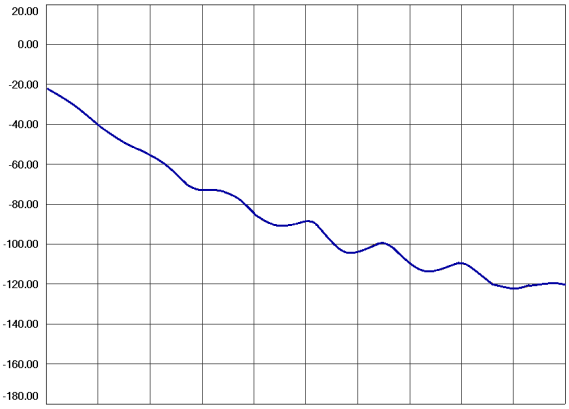

Figure 5.5: Phase of reflection coefficient at aperture ($\overline{S_{11}}$)-methanol-conical coaxial probe ($\alpha = 30\,^{\circ}$)[deg].

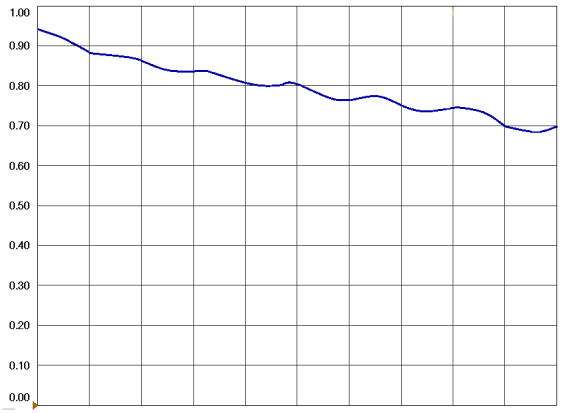

Figure 5.6: Amplitude of reflection coefficient at aperture ($\overline{S_{11}}$)-butanol-conical coaxial probe ($\alpha = 30\,^{\circ}$).

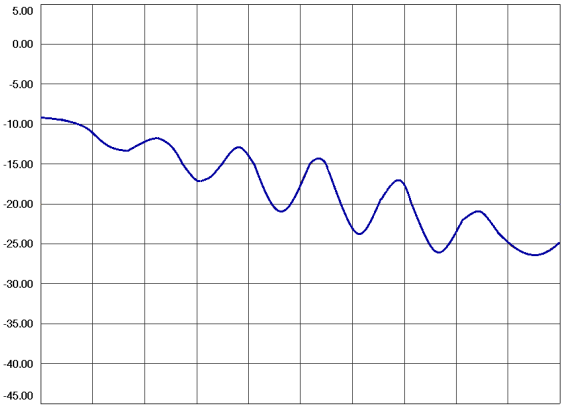

Figure 5.7: Phase of reflection coefficient at aperture ($\overline{S_{11}}$)-butanol-conical coaxial probe ($\alpha = 30\,^{\circ}$)[deg].

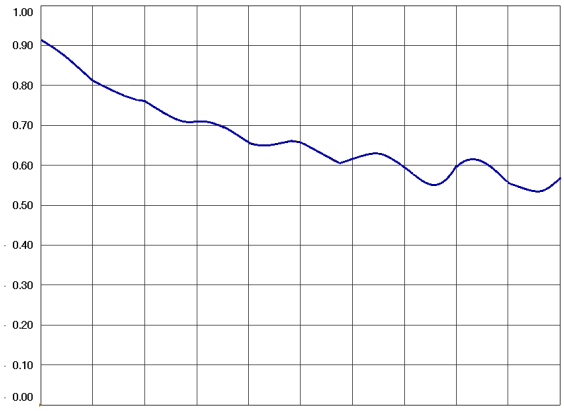

Figure 5.8: Amplitude of reflection coefficient at aperture ($\overline{S_{11}}$)-propanol-conical coaxial probe ($\alpha = 30\,^{\circ}$).

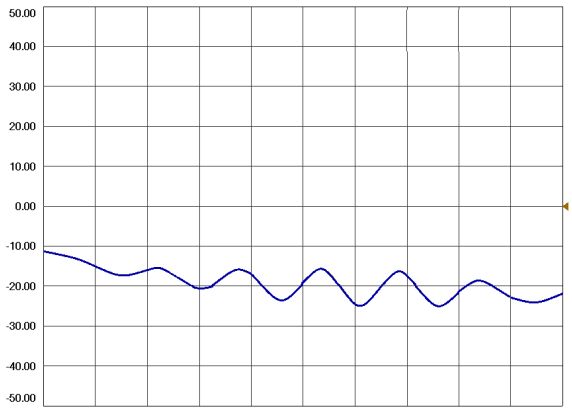

Figure 5.9: Phase of reflection coefficient at aperture ($\overline{S_{11}}$)-propanol-conical coaxial probe ($\alpha = 30\,^{\circ}$)[deg].

5.1.2 Dielectric constant

The dielectric properties of four different liquids, water, methanol, butanol and propanol were measured using the Agilent dielectric probe. This probe (model 85033E) measures the dielectric properties such as complex permittivity of many materials. The calibration of Agilent probe used a matched load, a short circuit and an open circuit states. Those results of Agilent probe, as the only references we have, show a good match between numerical results and measurement results. Figures. 5.10,5.11,5.12,5.13 show in sequence the relative permittivity and conductivity of water, methanol, butanol and propanol.

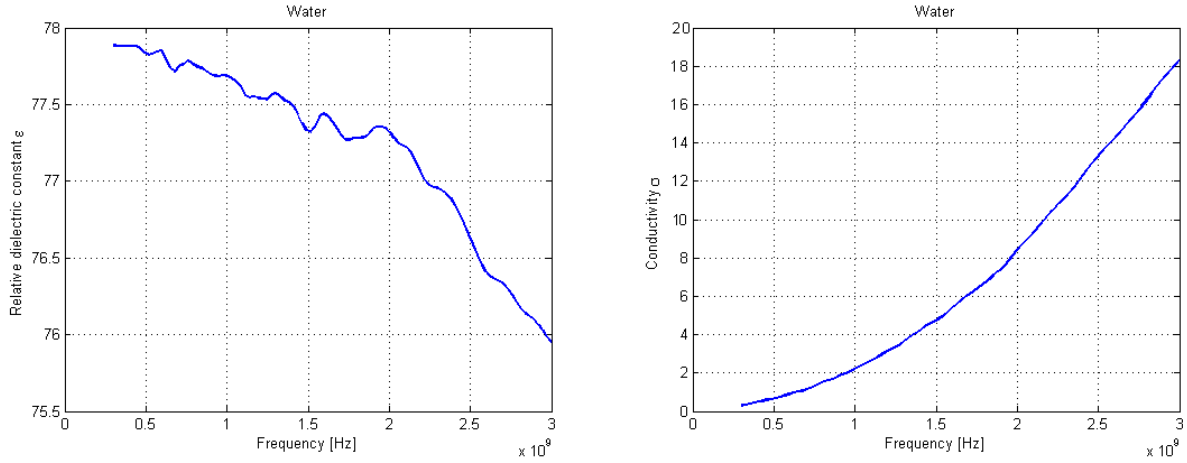

Figure 5.10: Relative permittivity and conductivity [S/m] of water- Measurements done with the 85033E Agilent probe.

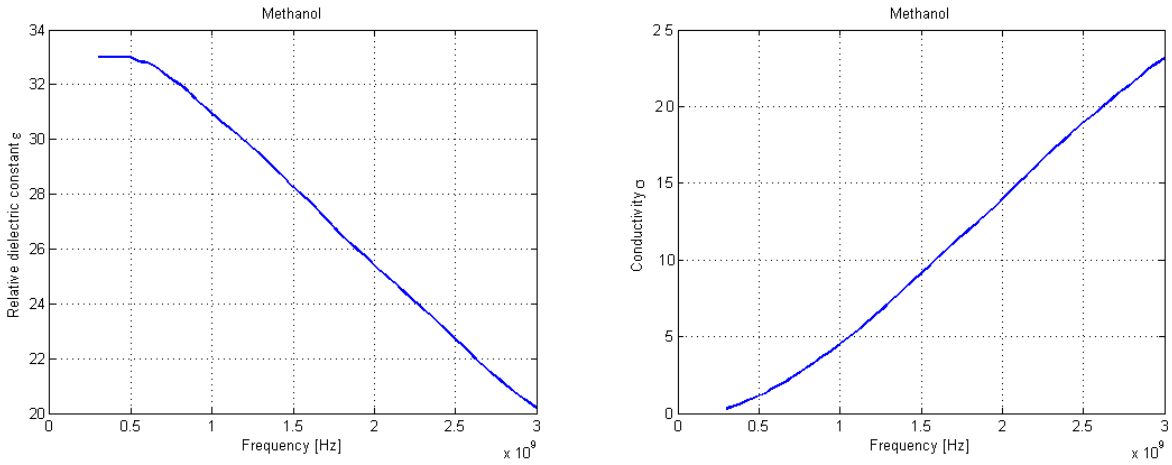

Figure 5.11: Relative permittivity and conductivity [S/m] of methanol- Measurements done with the 85033E Agilent probe.

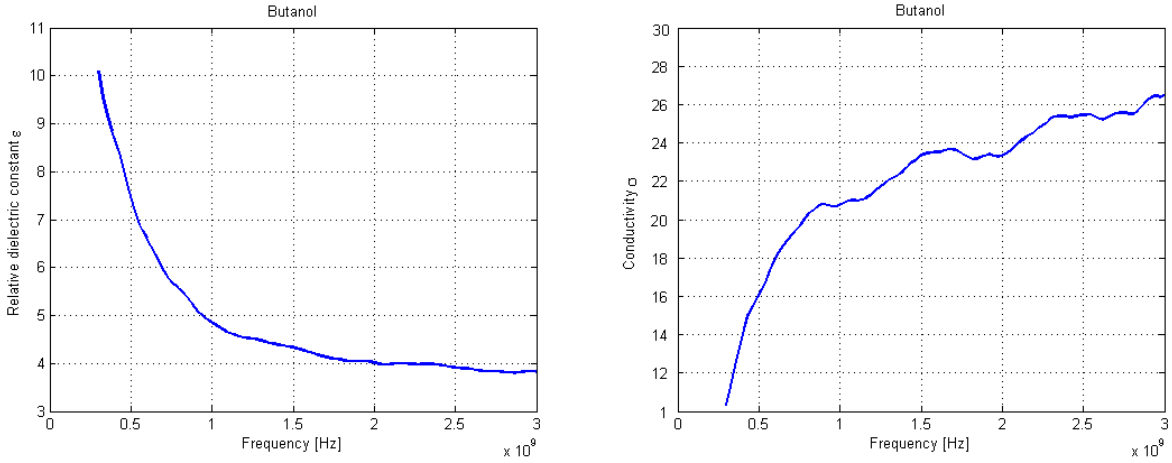

Figure 5.12: Relative permittivity and conductivity [S/m] of butanol- Measurements done with the 85033E Agilent probe.

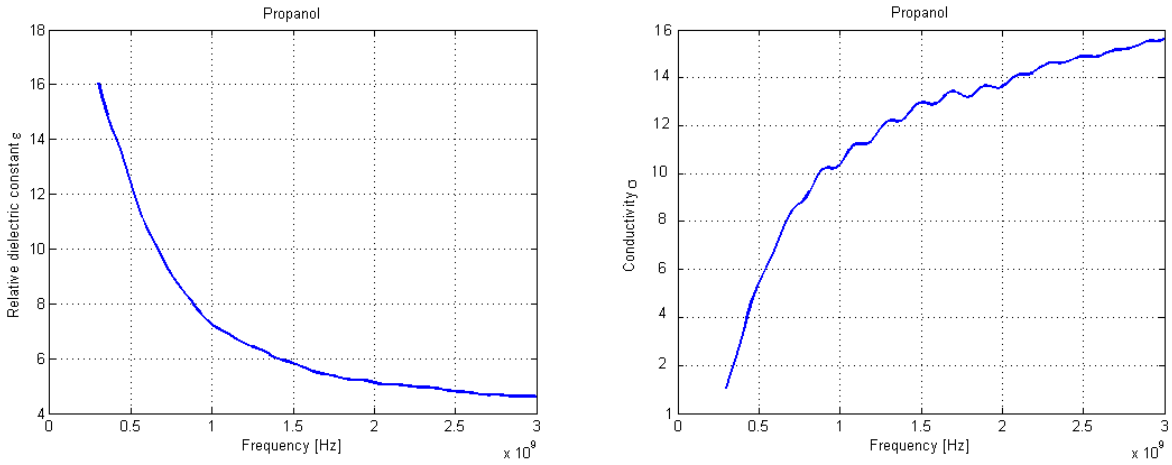

Figure 5.13: Relative permittivity and conductivity [S/m] of Propanol.

5.2 Comparison of the numerical and experimental results

As explained in Chapter 4, the best results are obtained by the improved virtual line model, Figures 5.14, 5.15, 5.16 compare the obtained experimental results and the simulation results of the improved virtual line model for methanol, ethanol and butanol.

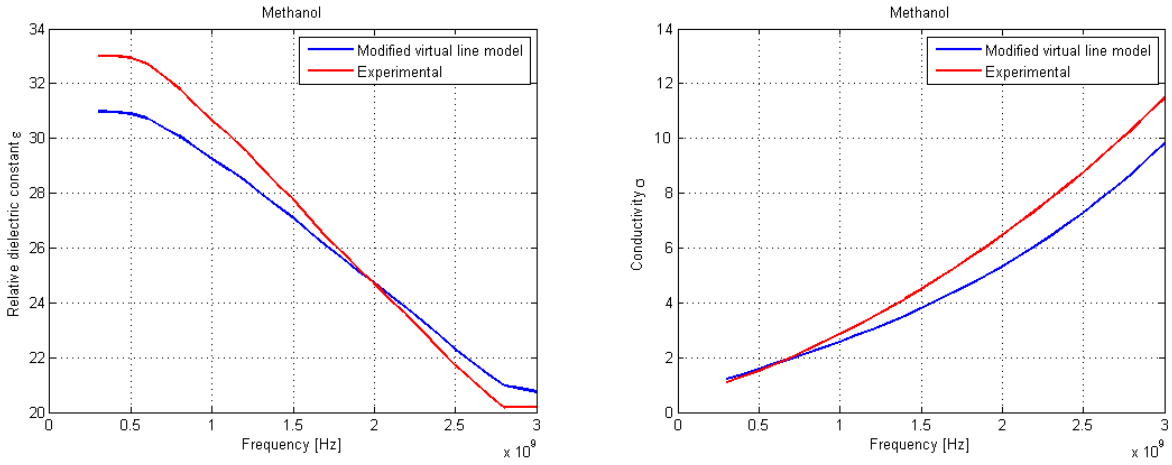

Figure 5.14: Comparison of relative permittivity and conductivity of methanol by experimental results by Agilent probe(red-Line) and improved virtual line method (Blue-Line).

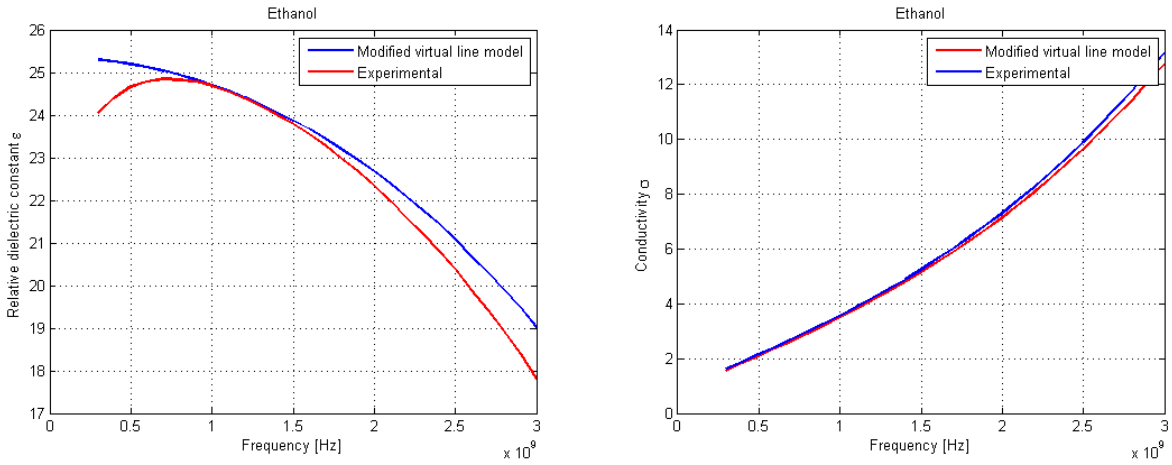

Figure 5.15: Comparison of relative permittivity and conductivity of ethanol by experimental results by Agilent probe(red-Line) and improved virtual line method (Blue-Line).

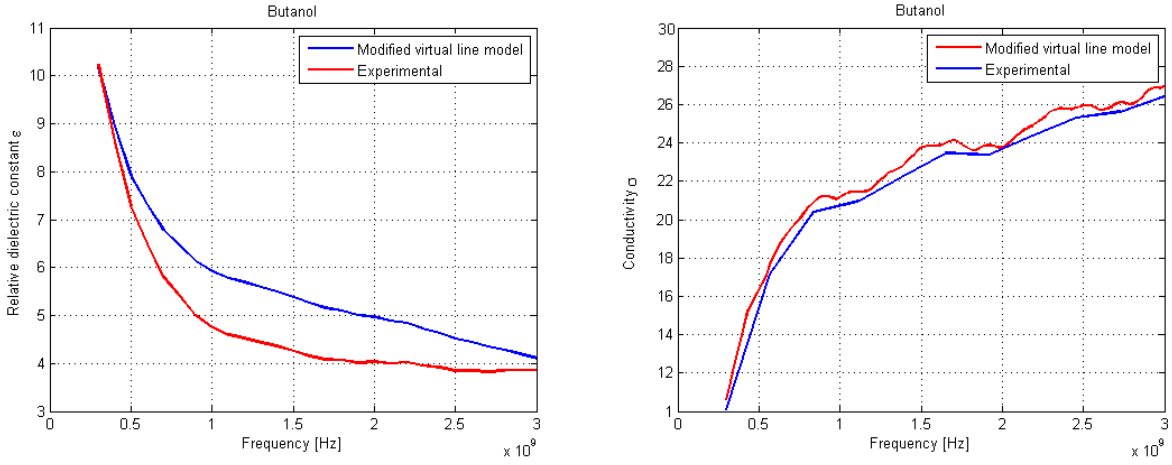

Figure 5.16: Comparison of relative permittivity and conductivity of butanol by experimental results by Agilent probe(red-Line) and improved virtual line method (Blue-Line).

Figures 5.15 and 5.16 compare the simulation results obtained from a improved virtual line model with the experimental results. The results assure the validity of improved virtual line model for modelling the conical- type open-ended coaxial probe and it is accurate enough.

5.3 Comparison of different types of probes

In this section, a comparative study of three different open-ended coaxial probes (flat, elliptic and conical type) is presented. The deduction of the permittivity of the material from the admittance data is made by assuming that the admittance of the material interface is described by an improved virtual line model. As discussed in chapter four, this model is

sufficiently robust to achieve precise results for lossy materials at microwave frequencies. By analysing the electric and magnetic field distribution at the probe aperture/material interface and determine the complex reflection coefficient, or scattering function S_{11}, at the connector of the different type open-ended coaxial line, the optimal probe type and configuration was determined as these are very important factor in both industrial and biological applications (measurements and microwave radiation treatment).

In Fig 5.17, the phases of $\overline{S_{11}}$ for different probes at different frequencies are shown which result in different impedances and then different sensitivities and accuracies. The amplitude of $\overline{S_{11}}$ for different probe is approximately the same.

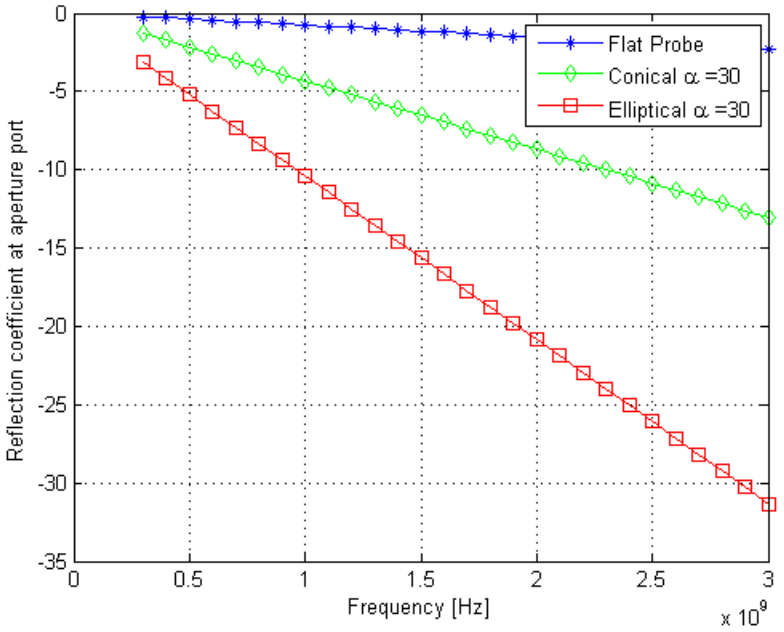

Figure 5.17: Phase of $\overline{S_{11}}$ for different probes (air).

As explained in chapter four, to calculate the dielectric constant by using improved virtual line method, the two constant D and y must be calculated. Figures 5.18-5.23 show these two constants for different types of probes.

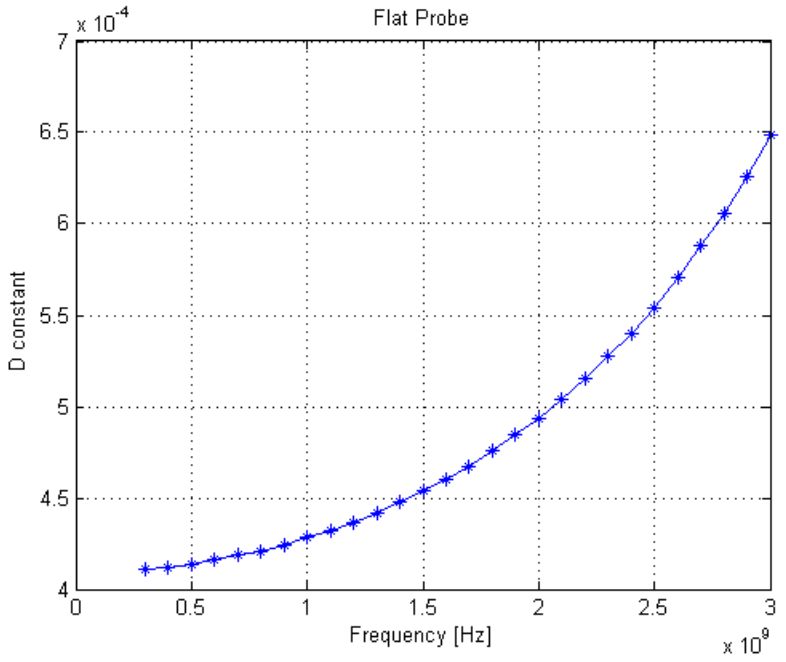

Figure 5.18: Virtual line model's length (D) for flat coaxial probe [m].

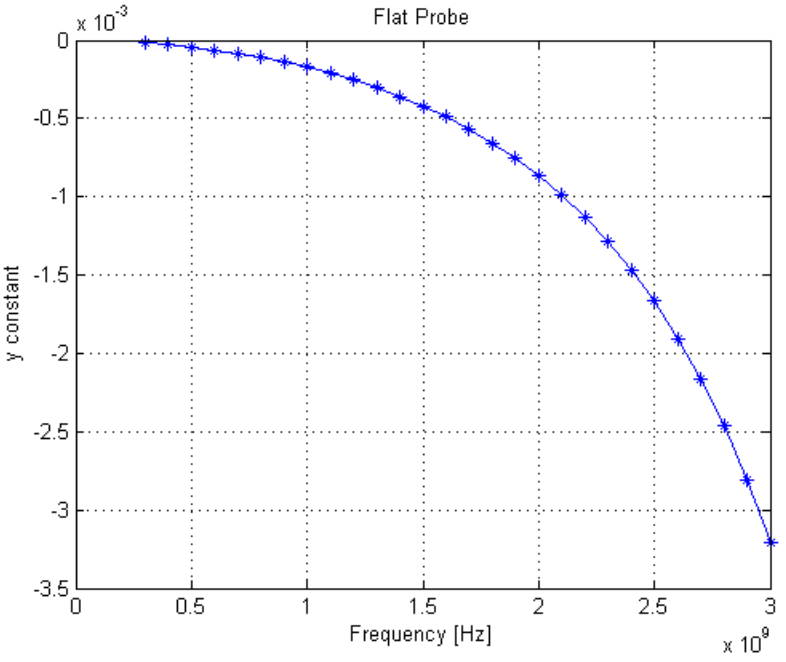

Figure 5.19: Virtual line model's y for flat coaxial probe.

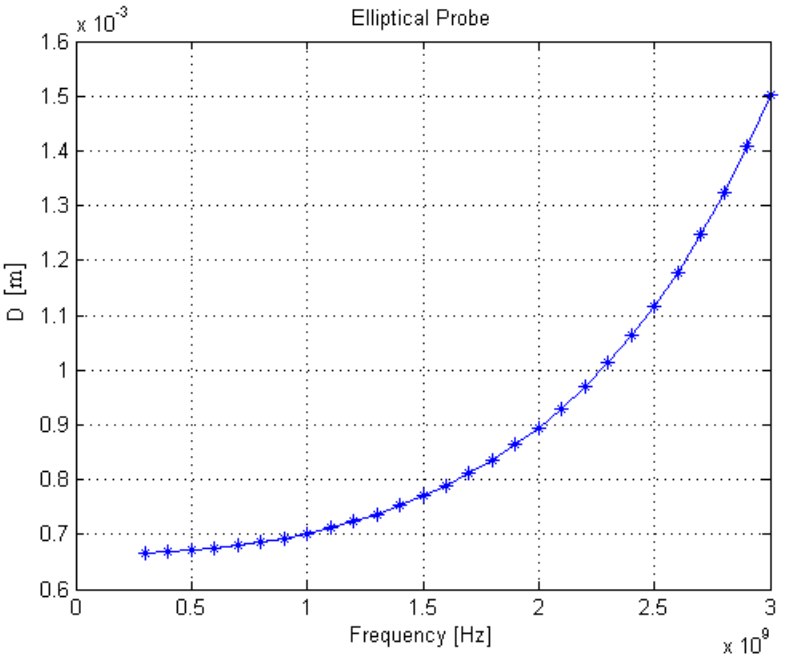

Figure 5.20: Virtual line model's length (D) for elliptical coaxial probe ($\alpha = 15\,^{\circ}$) [m].

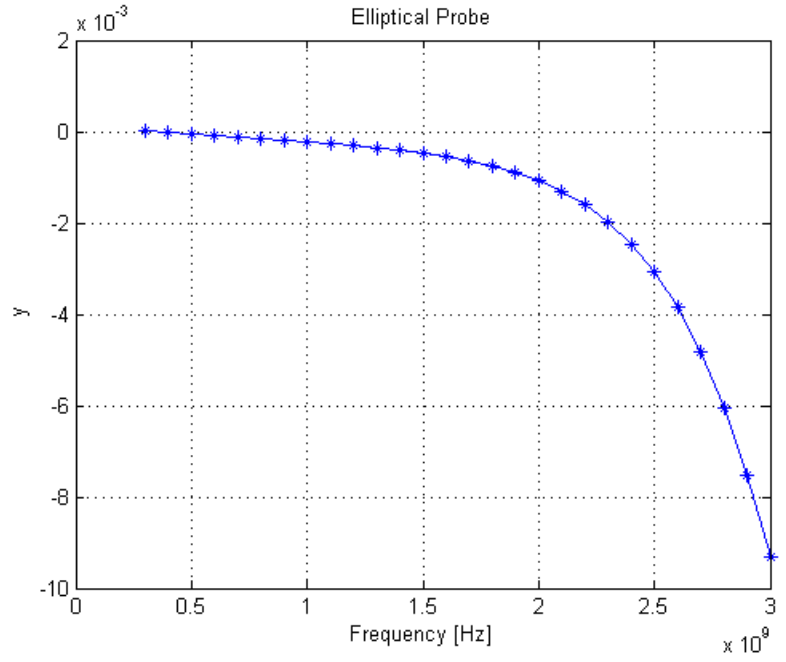

Figure 5.21: Virtual line model's y for elliptical coaxial probe ($\alpha = 15\,^{\circ}$).

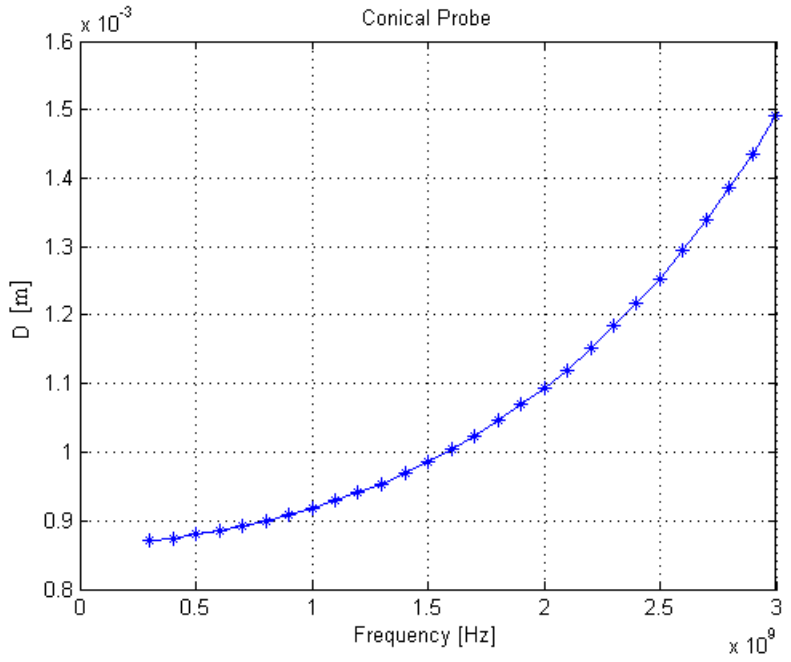

Figure 5.22: Virtual line model's length (D) for conical coaxial probe ($\alpha = 30\,°$)[m].

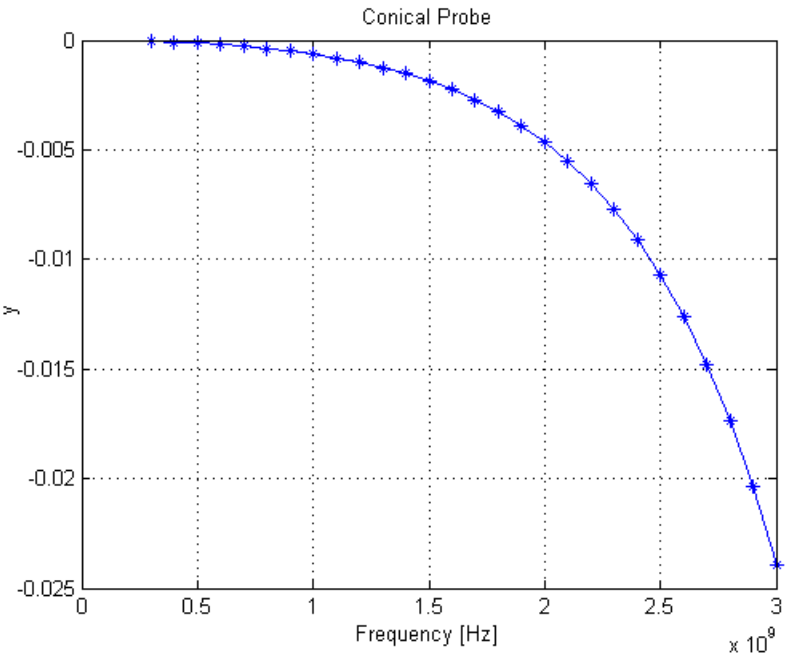

Figure 5.23: Virtual line model's y for conical coaxial probe ($\alpha = 30\,°$).

After the calculation of these parameters, we are able to determine the complex dielectric permittivity of a medium using equation 4.15. Figures 5.24, 5.26 and 5.28 show the complex permittivity profiles of Ethanol, Methanol and Butanol of flat, conical and elliptical coaxial

probes respectively and Figures 5.25, 5.27 and 5.29 show the conductivity profiles of Ethanol, Methanol and Butanol obtained with the flat, conical and elliptical coaxial probes respectively
.

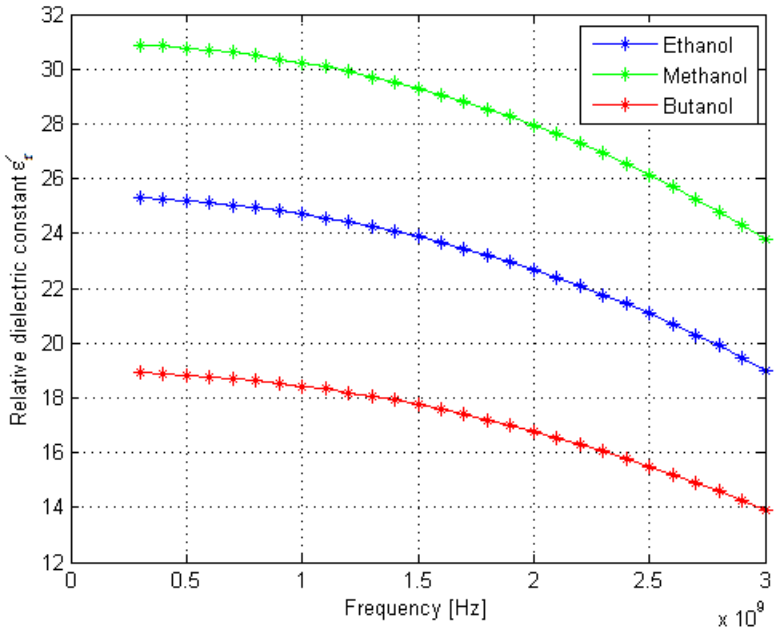

Figure 5.24: Relative permittivity profiles of ethanol, methanol and butanol-flat coaxial probe.

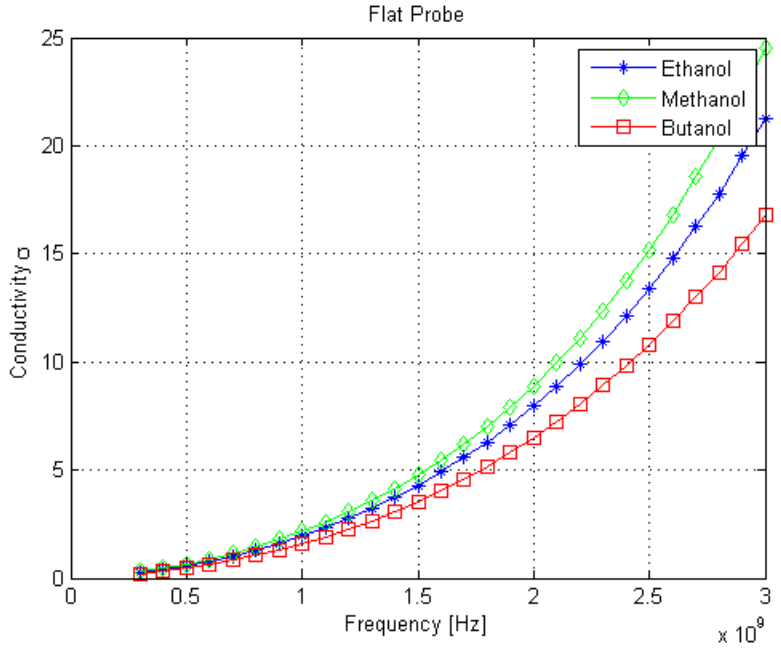

Figure 5.25: Conductivity profiles of ethanol, methanol and butanol-flat coaxial probe [S/m].

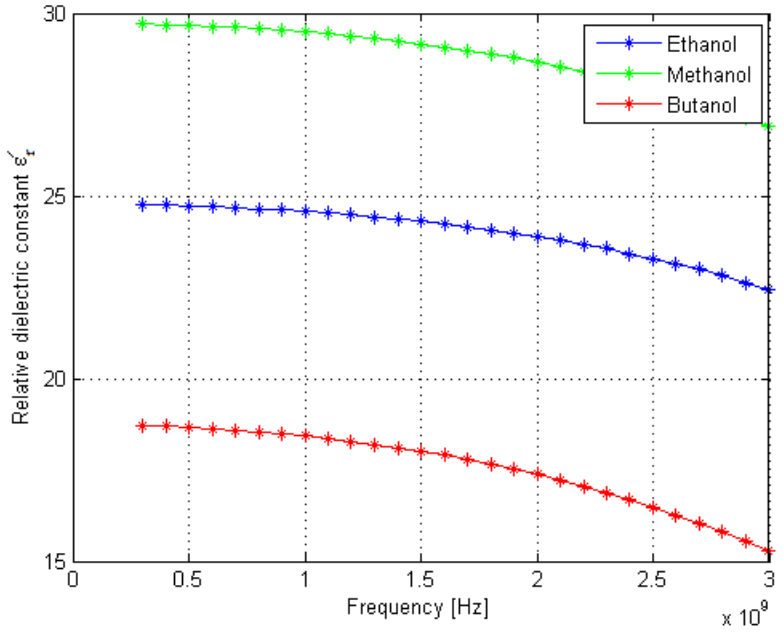

Figure 5.26: Relative permittivity profiles of ethanol, methanol and butanol-conical coaxial probe ($\alpha = 30\,^{\circ}$).

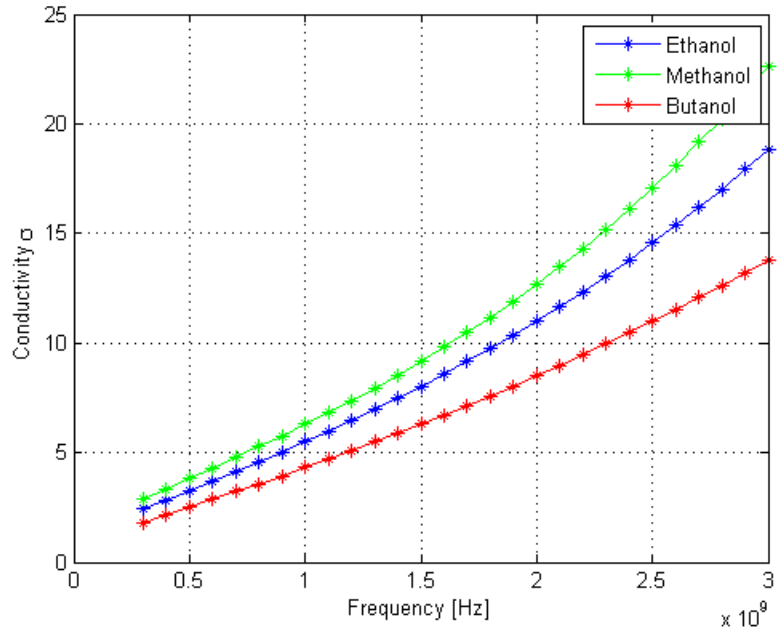

Figure 5.27: Conductivity profiles of ethanol, methanol and butanol-conical coaxial probe ($\alpha = 30\,^{\circ}$) [S/m].

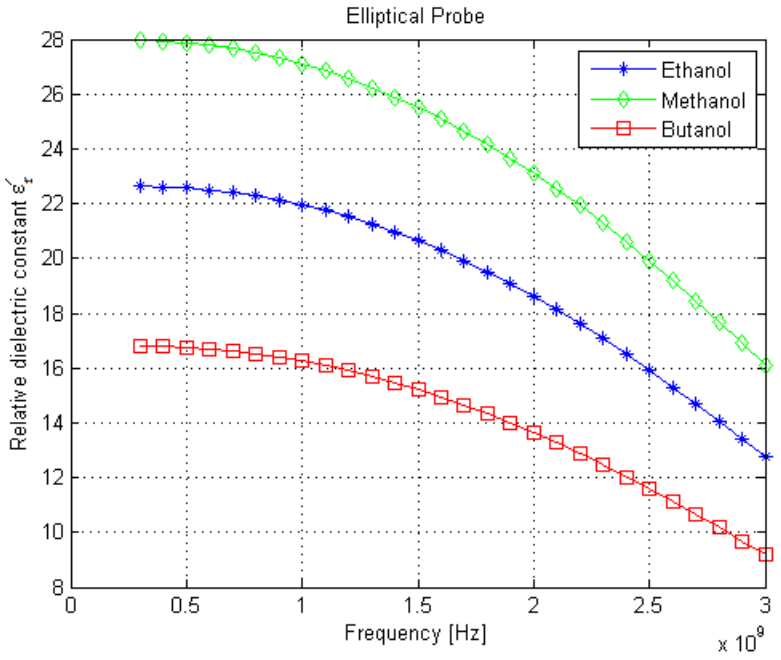

Figure 5.28: Relative permittivity profiles of ethanol, methanol and butanol-elliptical poaxial probe ($\alpha = 15\,°$).

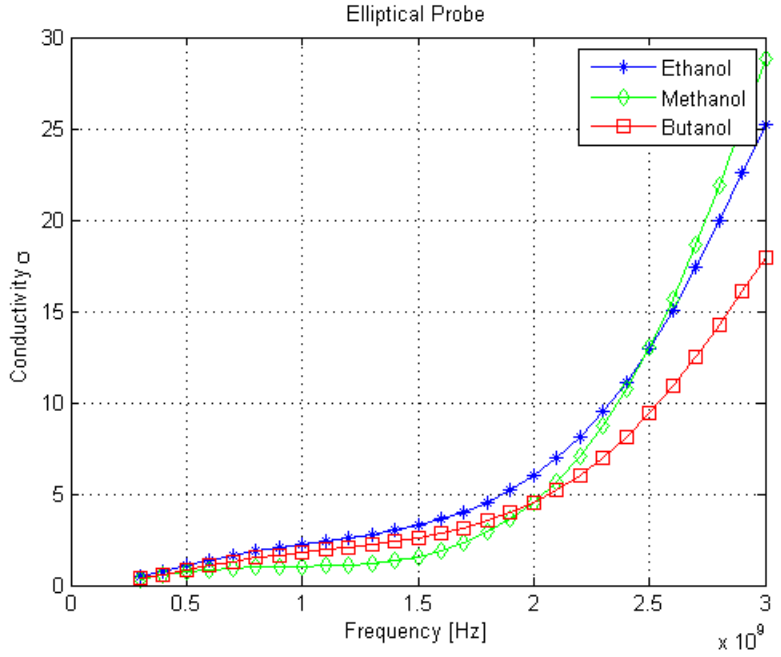

Figure 5.29: Conductivity profiles of ethanol, methanol and butanol-elliptical ($\alpha = 15\,°$) coaxial probe [S/m].

The results for these three different probes are approximately the same, only the sensitivity

increased for the elliptical and conical probes. In the next section we will demonstrate that the sharper angle for conical probe could result in better results.

5.4 Effect of cone angle of a conical type coaxial probe in dielectric measurement

In this part, the effect of using different cone angles of a conical type coaxial probe in measuring dielectric properties of materials is studied. Reflection coefficient impedance and dielectric permittivity of six different angles of an open ended coaxial lines are studied. Using probes of sharper cone angles (sharper tips) allows for easier penetration into wide range of biological tissue, which is an important feature in many biological applications. Fig. 5.30 show the sum of measured capacitance for cone part of coaxial probe body and fringing capacitances for various cone angles, α , of coaxial sensor.

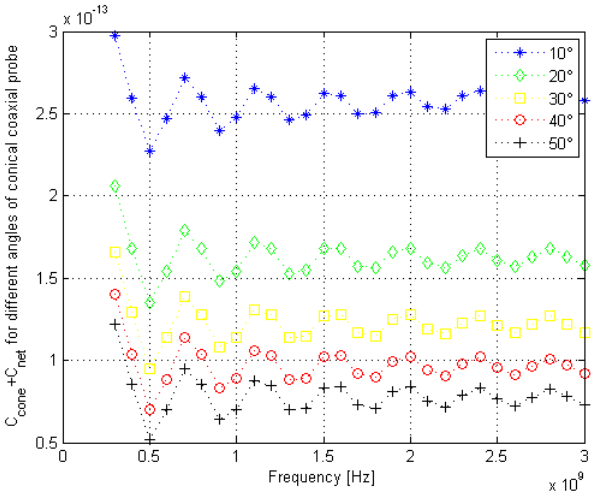

Figure 5.30: $C_{cone} + C_{net}$ for different angles of conical coaxial probe [F].

The results demonstrate that for sharper cone the capacitance increase and it is the main reason for the increase of accuracy and sensitivity. Small changes in properties of materials show more effect in sharper conical coaxial probe. Thus, open-ended conical coaxial probes can be successfully used especially at low frequencies with the advantage of increased accuracy and sensitivity for sharper angles. These results also allow the quantification the upper and lower frequency limit for different angles in which the conical type coaxial probe can be applied. Moreover, by analyzing the electric and magnetic fields distribution at the probe aperture material interface and determine the complex reflection coefficient, or scattering function S_{11}, at the connector of the conical type open-ended coaxial line, the optimal configuration for probe can be determined.

CHAPTER 6

CONCLUSIONS AND CONTRIBUTIONS

6.1 Conclusions

In this thesis, a numerical finite element method for studying the electric field and reflection coefficient of penetrable material using a new type of conical type coaxial probe has been presented. By analysing the electric field and magnetic field distributions at the probe aperture material interface, the complex reflection coefficient and impedance at the connector of the conical type open-ended coaxial line are determined. Consequently, three different conical-type open-ended coaxial probe models which relate the coaxial line end impedance to the complex permittivity of the material under test is presented. At the end, the effect of using different structures of probes with different angles in complex dielectric measurement is studied and reported. It can be concluded that the modified virtual line model gives more exact results in comparison to antenna and capacitance model, and that the advantages of conical type probes (specially probes of sharper cone angles or sharper tips) are not only in its easy insertion in material and biological applications, but also its accuracy and sensitivity improved in the low frequency range in comparison with the normal planes open ended coaxial probe.

6.2 Contributions

Parts of the results presented in this thesis are:

1. **Published Paper:**

   1. Arab, H and Akyel, C, "*Virtual transmission line of conical type coaxial open-ended probe for dielectric measurement*", International Journal of Advanced Technology in Engineering and Science (IJATES), Volume No.02, Issue No. 06, pp.365-372, June 2014.

2. **Accepted Paper:**

   2. Arab, H and Akyel, C, "*FEM analysis of conical type coaxial open-ended probe for dielectric measurement*", PIERS 2014 in Guangzhou, 25-27 August 2014.

   3. Arab, H and Akyel, C, "*Antenna Model of conical type coaxial open-ended probe for dielectric measurement*", International Conference on Advanced Technology and

Sciences (ICAT'14) in Turkey, 12-15 August 2014.

4. Arab, H and Akyel, C, "*Analysing the effect of conical coaxial probe angle in dielectric permittivity measurement*", 20th IMEKO TC4 International Symposium and 18th International Workshop in Italy, 15-17 September 2014.

5. Arab, H and Akyel, C, "*FEM analysis of elliptical type coaxial open-ended probe for dielectric measurement*", COMSOL Conference in Boston, 8-10 October 2014.

6. Arab, H and Akyel, C, "*Numerical measurement method of complex permittivity for a powdered material using a conical coaxial probe*", COMSOL Conference in Boston, 8-10 October 2014.

CHAPTER 7

FUTURE WORKS

As previously stated, the preceding work of this MSc.thesis, is only an intermediate step in the long run of the dielectric measurements. The future more advanced research may have the following contributions:

- Finding analytical solution for calculating electric field at aperture of conical probe.
- Finding a method to increase the accuracy and decreasing the memory storage of eigenvalue solver.
- Further investigation is required to more precisely determine the dependence of the error upon sample thickness and complex permittivity.
- While the coaxial open ended probe method works well for radio and microwave frequencies, it is not suitable for frequency range higher than 20 GHz. To alleviate these problems, alternative methods such as waveguide, resonator method are more attractive.
- Applying the methods used in this thesis for powdered materials or materials with nonlinear properties.
- More experiments, more simulations and more data processing have to be done on modelling of the probe, and to find an optimum algorithm for calculating dielectric properties of materials from a measured reflection coefficient.

REFERENCES

[1] G. Panariello, L. Verolino, and G. Vitolo, "Efficient and accurate full-wave analysis of the open-ended coaxial cable," *Microwave Theory and Techniques, IEEE Transactions on*, vol. 49, no. 7, pp. 1304–1309, 2001.

[2] N. Sheen and I. Woodhead, "An open-ended coaxial probe for broad-band permittivity measurement of agricultural products," *Journal of Agricultural Engineering Research*, vol. 74, no. 2, pp. 193–202, 1999.

[3] A. Kumbharkhane, "Time domain reflectometry technique for dielectric measurment," in *Physics and Engineering of Microwaves, Millimeter and Submillimeter Waves (MSMW), 2010 International Kharkov Symposium on*. IEEE, 2010, pp. 1–3.

[4] J. Sheen, "Microwave dielectric properties measurements using the waveguide reflection dielectric resonator," in *Instrumentation and Measurement Technology Conference Proceedings, 2007. IMTC 2007. IEEE*. IEEE, 2007, pp. 1–4.

[5] P. I. Dankov, "Two-resonator method for measurement of dielectric anisotropy in multilayer samples," *Microwave Theory and Techniques, IEEE Transactions on*, vol. 54, no. 4, pp. 1534–1544, 2006.

[6] G. Meunier, *The finite element method for electromagnetic modeling*. Wiley-ISTE, 2010.

[7] S. R. H. Hoole, *Finite elements, electromagnetics, and design*. Elsevier, 1995.

[8] Y. Kobayashi and M. Katoh, "Microwave measurement of dielectric properties of low-loss materials by the dielectric rod resonator method," *Microwave Theory and Techniques, IEEE Transactions on*, vol. 33, no. 7, pp. 586–592, 1985.

[9] D. Popovic and M. Okoniewski, "Precision open-ended coaxial probe for dielectric spectroscopy of breast tissue," in *Antennas and Propagation Society International Symposium, 2002. IEEE*, vol. 1. IEEE, 2002, pp. 815–818.

[10] W. J. Ellison and J.-M. Moreau, "Open-ended coaxial probe: Model limitations," *Instrumentation and Measurement, IEEE Transactions on*, vol. 57, no. 9, pp. 1984–1991, 2008.

[11] T. Marsland and S. Evans, "Dielectric measurements with an open-ended coaxial probe," in *IEE Proceedings H (Microwaves, Antennas and Propagation)*, vol. 134, no. 4. IET, 1987, pp. 341–349.

[12] J.-Z. Bao, M. L. Swicord, and C. C. Davis, "Microwave dielectric characterization of binary mixtures of water, methanol, and ethanol," *The Journal of chemical physics*, vol. 104, p. 4441, 1996.

[13] T. W. Athey, M. A. Stuchly, and S. S. Stuchly, "Measurement of radio frequency permittivity of biological tissues with an open-ended coaxial line: Part i," *Microwave Theory and Techniques, IEEE Transactions on*, vol. 30, no. 1, pp. 82–86, 1982.

[14] J. Galejs and J. R. Wait, "Antennas in inhomogeneous media," *American Journal of Physics*, vol. 37, p. 1164, 1969.

[15] J. A. Stratton, *Electromagnetic Theory*. New York: McGraw-Hill, 1941.

[16] E. Alanen, T. Lahtinen, and J. Nuutinen, "Measurement of dielectric properties of subcutaneous fat with open-ended coaxial sensors," *Physics in medicine and biology*, vol. 43, no. 3, p. 475, 1998.

[17] Y. Xu, F. Ghannouchi, and R. Bosisio, "Theoretical and experimental study of measurement of microwave permittivity using open ended elliptical coaxial probes," *Microwave Theory and Techniques, IEEE Transactions on*, vol. 40, no. 1, pp. 143–150, 1992.

[18] C. L. Pournaropoulos and D. K. Misra, "The co-axial aperture electromagnetic sensor and its application in material characterization," *Measurement Science and Technology*, vol. 8, no. 11, p. 1191, 1997.

[19] N. Wagner, M. Schwing, and A. Scheuermann, "Numerical 3-d fem and experimental analysis of the open-ended coaxial line technique for microwave dielectric spectroscopy on soil."

[20] P. Dabke, V. Prabhakar, and S. Sheppard, "Using features to support finite element idealizations," *Computers in Engineering*, vol. 1, pp. 183–183, 1994.

[21] J. Jin, *The finite element method in electromagnetics*. Wiley New York, 1993.

[22] I. A. Fanni, "Implementation in the *ANSYS* finite element code of the electric vector potential $t-\omega,\omega$ formulation and its validation with the magnetic vector potential A -V ,A formulation," Ph.D. dissertation, Universita Degli Studi di Cagliari, 2003.

[23] P. P. Silvester and R. L. Ferrari, *Finite elements for electrical engineers*. Cambridge university press, 1996.

[24] W. Ellison and J.-M. Moreau, "Open-ended coaxial probe: Model limitations," *Instrumentation and Measurement, IEEE Transactions on*, vol. 57, no. 9, pp. 1984–1991, Sept 2008.

[25] D. Popovic and M. Okoniewski, "Precision open-ended coaxial probe for dielectric spectroscopy of breast tissue," in *Antennas and Propagation Society International Symposium, 2002. IEEE*, vol. 1, 2002, pp. 815–818 vol.1.

[26] D. Popovic, L. McCartney, C. Beasley, M. Lazebnik, M. Okoniewski, S. Hagness, and J. Booske, "Precision open-ended coaxial probes for in vivo and ex vivo dielectric spectroscopy of biological tissues at microwave frequencies," *Microwave Theory and Techniques, IEEE Transactions on*, vol. 53, no. 5, pp. 1713–1722, May 2005.

[27] D. Popovic, L. McCartney, C. Beasley, and M. Lazebnik, "Precision open-ended coaxial probes for in vivo and ex vivo dielectric spectroscopy of biological tissues at microwave frequencies," *Microwave Theory and Techniques, IEEE Transactions on*, vol. 53, no. 9, pp. 3053–3053, Sept 2005.

[28] C. Gabriel, T. Chan, and E. Grant, "Admittance models for open ended coaxial probes and their place in dielectric spectroscopy," *Physics in medicine and biology*, vol. 39, no. 12, p. 2183, 1994.

[29] K. Folgerø and T. Tjomsland, "Permittivity measurement of thin liquid layers using open-ended coaxial probes," *Measurement Science and Technology*, vol. 7, no. 8, p. 1164, 1996.

[30] D. Berube, F. Ghannouchi, and P. Savard, "A comparative study of four open-ended coaxial probe models for permittivity measurements of lossy dielectric/biological materials at microwave frequencies," *Microwave Theory and Techniques, IEEE Transactions on*, vol. 44, no. 10, pp. 1928–1934, 1996.

[31] F. Lan, C. Akyel, F. Ghannouchi, J. Gauthier, and S. Khouaja, "A six-port based online measurement system using special probe with conical open end to determine relative complex permittivity at radio and microwave frequencies," in *Instrumentation and Measurement Technology Conference, 1999. IMTC/99. Proceedings of the 16th IEEE*, vol. 1. IEEE, 1999, pp. 42–47.

[32] G. Deschamps, "Impedance of an antenna in a conducting medium," *Antennas and Propagation, IRE Transactions on*, vol. 10, no. 5, pp. 648–650, 1962.

[33] M. Brandy, S. Symons, and S. Stuchly, "Dielectric behavior of selected animal tissues in vitro at frequencies from 2 to 4 ghz," *Biomedical Engineering, IEEE Transactions on*, no. 3, pp. 305–307, 1981.

[34] R. Keam and J. Holdem, "Permittivity measurements using a coaxial-line conical-tip probe," *Electronics Letters*, vol. 33, no. 5, pp. 353–355, 1997.

[35] Y.-S. Jo and S.-Y. Kim, "Fdtd validation on an improved virtual transmission-line conversion model of open-ended coaxial probe," in *Antennas and Propagation Society International Symposium, 2004. IEEE*, vol. 4. IEEE, 2004, pp. 4543–4546.

[36] T. Jakobsen and K. Folgerø, "Dielectric measurements of gas hydrate formation in water-in-oil emulsions using open-ended coaxial probes," *Measurement Science and Technology*, vol. 8, no. 9, p. 1006, 1997.

[37] B. McLaughlin and P. Robertson, "Miniature open-ended coaxial probes for dielectric spectroscopy applications," *Journal of Physics D: Applied Physics*, vol. 40, no. 1, p. 45, 2007.

ANNEXE A

HELMHOLTZ DIFFERENTIAL IN CYLINDRICAL COORDINATES

In Cylindrical Coordinates, the Helmholtz differential equation becomes:

$$\frac{1}{r}\frac{\partial}{\partial r}\left(r\frac{\partial \Psi}{\partial r}\right)+\frac{1}{r^2}\frac{\partial^2 \Psi}{\partial \theta^2}+\frac{1}{Z}\frac{\partial^2 \Psi}{\partial z^2}+k^2=0. \tag{A.1}$$

We use the method of separation:

$$\Psi(r,\theta,z)=R(r)\Phi(\varphi)Z(z); \tag{A.2}$$

$$\frac{1}{rR}\frac{\partial}{\partial r}\left(r\frac{\partial R}{\partial r}\right)+\frac{1}{r^2\Phi}\frac{\partial^2 \Phi}{\partial \varphi^2}+\frac{1}{Z}\frac{\partial^2 Z}{\partial z^2}+k^2=0. \tag{A.3}$$

The third term is independent of r and φ so it must be constant:

$$\frac{\mathrm{d}^2 Z}{\mathrm{d}z^2}=k_z^2 Z \Longrightarrow Z(z)=A_n e^{-ik_z z}+B_n e^{ik_z z}; \tag{A.4}$$

$$\frac{1}{rR}\frac{\partial}{\partial r}\left(r\frac{\partial \phi}{\partial r}\right)+\frac{1}{r^2\Phi}\frac{\partial^2 \Phi}{\partial \varphi^2}+\frac{1}{Z}\frac{\partial^2 Z}{\partial z^2}+(k^2-k_z^2)=0. \tag{A.5}$$

By defining $k_\rho=k^2-k_z^2$ and multiplying the resulting equation by r^2 to find:

$$\frac{r}{R}\frac{\partial}{\partial r}\left(r\frac{\partial R}{\partial r}\right)+\frac{1}{\Phi}\frac{\partial^2 \Phi}{\partial \varphi^2}+\frac{1}{Z}\frac{\partial^2 Z}{\partial z^2}+k_\rho^2 r^2=0. \tag{A.6}$$

The second term is independent of r and z, so we let:

$$\frac{\partial^2 \Phi}{\partial \varphi^2}=-\nu^2\Phi \Longrightarrow \Phi(\varphi)=\Phi_m(\varphi)=A_m e^{i\nu\varphi}, \quad m=0,\pm1,\pm2,... \tag{A.7}$$

as Φ is periodic or finite so that $\Phi(\varphi+2\pi)=\Phi(\varphi)$thus $m\in Z$. We also obtain the following expression for R component:

$$r\frac{\partial}{\partial r}\left(r\frac{\partial R}{\partial r}\right)+(k_\rho^2 r^2-\nu^2)R=0. \tag{A.8}$$

This can be rewritten as:

$$r^2\frac{\partial^2 R}{\partial r^2}+r\frac{\partial R}{\partial r}+(k_\rho^2 r^2-\nu^2)R=0, \tag{A.9}$$

which is Bessel's equation. Substituting back, the general solution is given by

$$R(r) = BJ_\nu(kr) + CY_\nu(kr), \tag{A.10}$$

where J_ν, denotes a Bessel function of the first kind and $Y_\nu(kr)$ denotes a Bessel functions of the second kind order ν.

$$J_\nu(kr) = \sum_{m=0}^{\infty} \frac{(-1)^m}{m!\,\Gamma(m+\nu+1)} \left(\frac{kr}{2}\right)^{2m+\nu}; \tag{A.11}$$

$$Y_\nu(kr) = \frac{J_\alpha(kr)\cos(\alpha\pi) - J_{-\nu}(kr)}{\sin(\nu\pi)}, \tag{A.12}$$

where $\Gamma(z)$ is the gamma function, a shifted generalization of the factorial function to non-integer values.

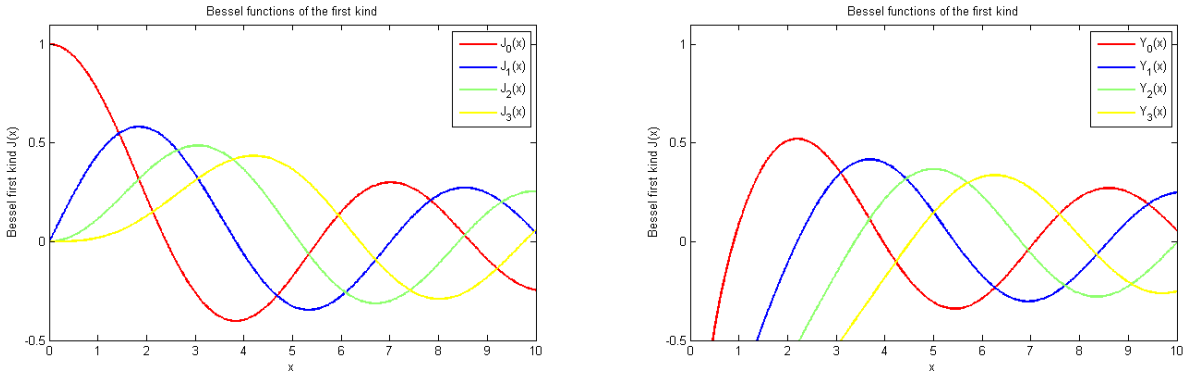

(a) Bessel functions of first kind.

(b) Bessel functions of Second kind.

Figure A.1: Bessel Functions

ANNEXE B

NODAL ELEMENTS

The domain is discretized into elements and over each element we assume a trial function which is properly an interpolation function. If linear triangular elements are used, the unknown function E within each element is approximated as:

$$E^e = a^e + b^e x + c^e y, \tag{B.1}$$

where a^e, b^e, c^e must be determined, and e is the element number. For a linear triangular

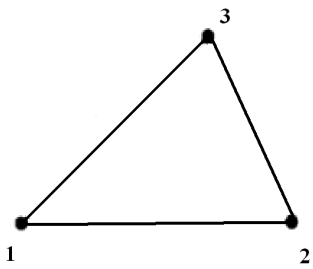

Figure B.1: Triangular element with first order nodal elements

element, on the node located at the vertices of the triangle the corresponding **E** denoted by E_1^e, E_2^e, E_3^e. Enforcing B.1 at the three nodes, we obtain:

$$E_1^e = a^e + b^e x_1^e + c^e y_1^e; \tag{B.2}$$

$$E_2^e = a^e + b^e x_2^e + c^e y_2^e; \tag{B.3}$$

$$E_3^e = a^e + b^e x_3^e + c^e y_3^e, \tag{B.4}$$

where x_j^e and y_j^e are the coordinate values of the J_{th} node. Solving for the constant coefficients a^e, b^e and c^e in terms of E_j^e, and substituting them back into B.1 yields:

$$E^e(x, y) = \sum_{i=1}^{3} N_j^e(x, y) E_j^e, \tag{B.5}$$

where $N_j^e(x,y)$ are the interpolation functions given by:

$$N_j^e(x,y) = \frac{1}{\Delta^e}(a_j^e + b_j^e x + c_j^e y); \tag{B.6}$$

$$\Delta^e = 1/2 \begin{pmatrix} 1 & x_1^e & y_1^e \\ 1 & x_2^e & y_2^e \\ 1 & x_3^e & y_3^e \end{pmatrix} = 1/2(b_1^e c_2^e - b_2^e c_1^e), \tag{B.7}$$

and

$$\begin{cases} a_1^e = x_2^e y_3^e + y_2^e x_3^e & b_1^e = y_2^e + y_3^e & c_1^e = x_3^e + x_2^e \\ a_2^e = x_3^e y_1^e + y_3^e x_1^e & b_2^e = y_3^e + y_1^e & c_2^e = x_1^e + x_3^e \\ a_3^e = x_1^e y_2^e + y_1^e x_2^e & b_3^e = y_1^e + y_2^e & c_3^e = x_2^e + x_1^e \end{cases} . \tag{B.8}$$

By substituting Equation B.5 in Equation 3.4:

$$\frac{\partial F^e(E^e)}{\partial E^e} = \sum_{i=1}^{3} E_z^e \iint \Big(\mu^{-1}\big(\frac{\partial N_i^e}{\partial x}\frac{\partial N_j^e}{\partial x} + \frac{\partial N_i^e}{\partial y}\frac{\partial N_j^e}{\partial y}\big) - k_0^2 \varepsilon N_i^e N_j^e\Big) d\Omega, \tag{B.9}$$

which can be written in matrix form as:

$$\frac{\partial F^e(E^e)}{\partial E^e} = K^e E^e, \tag{B.10}$$

where

$$K^e = \iint_\Omega \Big(\mu_r^{-1}\frac{\partial N_i^e}{\partial x}\frac{\partial N_j^e}{\partial x} + \mu_r^{-1}\frac{\partial N_i^e}{\partial y}\frac{\partial N_j^e}{\partial y} - k_0^2 \varepsilon N_i^e N_j^e\Big) d\Omega, \tag{B.11}$$

K^e is a symmetric matrix. By using the formula:

$$\iint_\Omega (N_1^e)^l (N_2^e)^m (N_3^e)^n d\Omega = \frac{l!m!n!}{l+m+n+2} 2\Delta^e, \tag{B.12}$$

equations B.9 become:

$$K^e = \frac{1}{4\Delta^e}\mu_r^{-1}(b_i^e b_j^e + c_i^e c_j^e) + \frac{\Delta^e}{12} k_0^2 \varepsilon (1 + \delta_{ij}) \tag{B.13}$$

ANNEXE C

EDGE ELEMENT

Triangular elements are used because they are applicable in different classes of geometry. Refer to triangular in figure C.1 the form of basis function is:

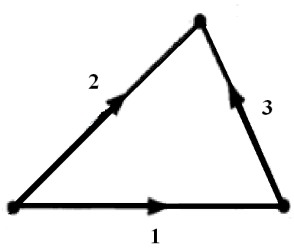

Figure C.1: Triangular element with linear edge and first order nodal elements

$$\mathbf{W}_{12} = N_1^e \nabla N_2^e - N_2^e \nabla N_1^e; \tag{C.1}$$

$$\mathbf{W}_{13} = N_1^e \nabla N_3^e - N_3^e \nabla N_1^e; \tag{C.2}$$

$$\mathbf{W}_{23} = N_2^e \nabla N_3^e - N_3^e \nabla N_2^e; \tag{C.3}$$

$$N_j^e(x,y) = \frac{1}{2\Delta^e}(a_j^e + b_j^e x + c_j^e y); \tag{C.4}$$

$$\mathbf{E}^e(x,y) = \sum_{i=1}^{3} \mathbf{N}_j^e(x,y) E_j^e; \tag{C.5}$$

$$\mathbf{N}_1^e = \mathbf{W}_{12} l_1^e; \quad \mathbf{N}_2^e = \mathbf{W}_{13} l_2^e; \quad \mathbf{N}_3^e = \mathbf{W}_{23} l_3^e, \tag{C.6}$$

where l_i^e denote the length of the edge connecting two nodes, and it is not difficult to see that:

$$\nabla \cdot \mathbf{W}_{12} = \nabla \cdot (N_1^e \nabla N_2^e) - \nabla \cdot (N_2^e \nabla N_1^e) = 0; \tag{C.7}$$

$$\mathbf{W}_{13} = N_1^e \nabla N_3^e - N_3^e \nabla N_1^e; \tag{C.8}$$

$$\nabla \times \mathbf{W}_{23} = \nabla \times (N_2^e \nabla N_3^e) - \nabla \times (N_3^e \nabla N_2^e) = 2\nabla N_1^e \times \nabla N_2^e = \frac{l_i^e l_j^e}{\Delta^e}, \tag{C.9}$$

where $N_j^e(x,y)$ are the interpolation functions given by:

$$\Delta^e = 1/2 \begin{pmatrix} 1 & x_1^e & y_1^e \\ 1 & x_2^e & y_2^e \\ 1 & x_3^e & y_3^e \end{pmatrix} = \frac{1}{2}(b_1^e c_2^e - b_2^e c_1^e), \tag{C.10}$$

and

$$\begin{cases} a_1^e = x_2^e y_3^e + y_2^e x_3^e & b_1^e = y_2^e + y_3^e & c_1^e = x_3^e + x_2^e \\ a_2^e = x_3^e y_1^e + y_3^e x_1^e & b_2^e = y_3^e + y_1^e & c_2^e = x_1^e + x_3^e \\ a_3^e = x_1^e y_2^e + y_1^e x_2^e & b_3^e = y_1^e + y_2^e & c_3^e = x_2^e + x_1^e \end{cases}$$

Typical element matrix resulting form the discretization of a vector wave equation contain integrals of the following forms:

$$E_{ij}^e = \iint (\nabla \times \mathbf{N}_i^e)(\nabla \times \mathbf{N}_j^e) d\Omega; \tag{C.11}$$

$$F_{ij}^e = \iint \mathbf{N}_i^e \cdot \mathbf{N}_j^e d\Omega; \tag{C.12}$$

$$H_{ij}^e = \iint \mathbf{N}_i^e (\nabla \times N_j^e) d\Omega. \tag{C.13}$$

In the above equations $\mathbf{N}_i^e$ denote edge basis functions and N_i^e denote nodal basis functions. Hence, $\nabla \times \mathbf{N}_i^e = \overline{k} \frac{l_i^e}{\Delta^e}$ the matrix E_{ij}^e can be calculated very simple,

$$E_{ij}^e = \frac{l_i^e l_j^e}{\Delta^e}. \tag{C.14}$$

For calculating F_{ij}^e and H_{ij}^e by using the formula:

$$\iint_\Omega (N_1^e)^l (N_2^e)^m (N_3^e)^n d\Omega = \frac{l!m!n!}{l+m+n+2} 2\Delta^e. \tag{C.15}$$

Equations C.12 become:

$$F^e_{11} = \frac{l^e_1 l^e_1}{24\Delta^e}(f_{22} - f_{12} + f_{11}); \tag{C.16}$$

$$F^e_{12} = \frac{l^e_1 l^e_2}{48\Delta^e}(f_{23} - f_{22} + 2f_{13} + f_{12}); \tag{C.17}$$

$$F^e_{13} = \frac{l^e_1 l^e_3}{48\Delta^e}(f_{21} - 2f_{23} - f_{11} + f_{13}); \tag{C.18}$$

$$F^e_{22} = \frac{l^e_2 l^e_2}{24\Delta^e}(f_{33} - f_{23} + f_{22}); \tag{C.19}$$

$$F^e_{23} = \frac{l^e_2 l^e_3}{48\Delta^e}(f_{31} - 2f_{21} - f_{33} + f_{23}); \tag{C.20}$$

$$F^e_{33} = \frac{l^e_3 l^e_3}{24\Delta^e}(f_{11} - f_{13} + f_{33}), \tag{C.21}$$

and for that part inclded nodal and edge elements in equation we obtained :

$$H^e_{11} = \frac{l^e_1}{12\Delta^e}(f_{21} - f_{11}); \tag{C.22}$$

$$H^e_{12} = \frac{l^e_1}{12\Delta^e}(f_{22} - f_{12}); \tag{C.23}$$

$$H^e_{13} = \frac{l^e_1}{12\Delta^e}(f_{23} - f_{13}); \tag{C.24}$$

$$H^e_{21} = \frac{l^e_1}{12\Delta^e}(f_{31} - f_{21}); \tag{C.25}$$

$$H^e_{22} = \frac{l^e_1}{12\Delta^e}(f_{32} - f_{22}); \tag{C.26}$$

$$H^e_{23} = \frac{l^e_1}{12\Delta^e}(f_{33} - f_{23}); \tag{C.27}$$

$$H^e_{31} = \frac{l^e_1}{12\Delta^e}(f(_{11} - f_{31}); \tag{C.28}$$

$$H^e_{32} = \frac{l^e_1}{12\Delta^e}(f_{12} - f_{32}); \tag{C.29}$$

$$H^e_{33} = \frac{l^e_1}{12\Delta^e}(f_{13} - f_{33}), \tag{C.30}$$

$$\tag{C.31}$$

where f_{ij} defined as:

$$f_{ij} = b^e_i b^e_j + c^e_i c^e_j. \tag{C.32}$$

.

```
% ------------------------------------------------------------
% Compute element matrix for a triangle and its node basis first order
% ------------------------------------------------------------
function [A,B]= nodefirstorderFEM2D
[xy, n, noNum,ne]=unimesh01;
x=xy(1,:);
y=xy(2,:);
Ae=zeros(3);
A=zeros(noNum);
B=zeros(noNum);
del_ij=eye(3);
for e=1:ne
    ii=n(1,e);
    jj=n(2,e);
    m=n(3,e);
    be(1)=y(jj)-y(m);
    be(2)=y(m)-y(ii);
    be(3)=y(ii)-y(jj);
    ce(1)=x(m)-x(jj);
    ce(2)=x(ii)-x(m);
    ce(3)=x(jj)-x(ii);
    Deltae=abs(0.5*(be(1)*ce(2)-be(2)*ce(1)));
    for i=1:3
        for j=1:3
            Ae(i,j)=1/(4*Deltae)*(be(i)*be(j)+ce(i)*ce(j));
        end
    end
    Be=Deltae*1/12*(1+del_ij);
    no =n(:,e);
%Compute the element matrix and add the contribution to the global matrix.
    A(no,no) = A(no,no) + Ae;
    B(no,no) = B(no,no) + Be;
end
% % %%
%Baundary condition
load('figdata','e');
ee1=e([1 2],:);
nbc=unique(ee1(:));


for i=1:size(nbc)
%     A(nbc(i),nbc(i))=1;
%     B(nbc(i),nbc(i))=1;
```

```
    for j=1:noNum
        if(j~=nbc(i))
%             A(nbc(i),j)=0;
                        A(j,nbc(i))=0;
%             B(nbc(i),j)=0;
                        B(j,nbc(i))=0;
        end
    end
end


[xv,kz2,iresult]=sptarn(A,B,1,100);
kz=sqrt((kz2));
% sol=xv(:,75);
% % plot(kz,'*')
figure(2); plot(kz,'--rs','LineWidth',2,...
                'MarkerEdgeColor','k',...
                'MarkerFaceColor','b',...
                'MarkerSize',5)
           xlabel('string')
xlabel({'mode[-]';'Cut off Wave Number for Circular waveguide'})
ylabel('kz')
title('First Orde Nodal FEM')
end


function [E,F,el2ed]=edgFEM2D55
clc
clear all
close all
[p, n, ~,ne]=unimesh01;
x=p(1,:);
y=p(2,:);
%%
el2no = sort(n);
n1 = el2no([1 1 2],:);
n2 = el2no([2 3 3],:);
[~,~,el2ed] = unique([n1(:) n2(:)],'rows');
el2ed = reshape(el2ed,3,size(el2no,2));
lll=el2ed';
l=zeros(ne,3);
n=el2no';
```

```
for e5=1:ne
    l(e5,1)=sqrt((x(n(e5,2))-x(n(e5,1)))^2+(y(n(e5,2))-y(n(e5,1)))^2);
    l(e5,2)=sqrt((x(n(e5,3))-x(n(e5,1)))^2+(y(n(e5,3))-y(n(e5,1)))^2);
    l(e5,3)=sqrt((x(n(e5,3))-x(n(e5,2)))^2+(y(n(e5,3))-y(n(e5,2)))^2);
end
%%
r=max(max(el2ed));
l=l';

%%%%%%%%%%%%%%%%%%%%%%%% EDGE ELEMENTS CODE %%%%%%%%%%%%%%%%%%%%%%%%%
E=zeros(r);
F=zeros(r);
Ee1=zeros(3);
Fe=zeros(3);
n=n';
for e6=1:ne
    ii=n(1,e6);
    jj=n(2,e6);
    m=n(3,e6);
    be(2)=y(m)-y(ii);
    be(3)=y(jj)-y(ii);
    ce(2)=x(m)-x(ii);
    ce(3)=x(jj)-x(ii);
    Deltae=abs(0.5*(be(2)*ce(3)-be(3)*ce(2)));
    f(2,2)=be(2)*be(2)+ce(2)*ce(2);
    f(2,3)=-(be(2)*be(3)+ce(2)*ce(3));
    f(3,3)=be(3)*be(3)+ce(3)*ce(3);

    for i=1:3
        for j=1:3

            Ee1(i,j)=(l(i,e6)*l(j,e6))/Deltae;
        end
    end
    Fe(1,1)=l(1,e6)*l(1,e6)/(24*(Deltae))*(3*f(2,2)+3*f(2,3)+f(3,3));
    Fe(1,2)=l(2,e6)*l(1,e6)/(24*(Deltae))*(3*f(2,3)+f(2,2)+f(3,3));
    Fe(1,3)=l(3,e6)*l(1,e6)/(24*(Deltae))*(f(2,3)-f(2,2)+f(3,3));
    Fe(2,2)=l(2,e6)*l(2,e6)/(24*(Deltae))*(3*f(3,3)+3*f(2,3)+f(2,2));
    Fe(2,3)=l(2,e6)*l(3,e6)/(24*(Deltae))*(f(3,3)-f(2,3)-f(2,2));
    Fe(3,3)=l(3,e6)*l(3,e6)/(24*(Deltae))*(f(2,2)-f(2,3)+f(3,3));
    Ee=Ee1.*[1 -1 1;-1 1 -1;1 -1 1];
    for xx=1:3
        for yy=1:3
            Fe(yy,xx)=Fe(xx,yy);
```

```
        end
    end

    %%assemble
    no=el2ed(:,e6);
    E(no,no)=E(no,no)+Ee;
    F(no,no)=F(no,no)+Fe;

end
%Baundary condition
load('figdata','e');
bcedg=zeros(1,size(e,2));
 el2ed3=el2ed(:)';
 pp=size(el2ed3,2);
 c=1;
for i=1:pp
    [vv,~,~]=find(el2ed3==el2ed3(1,i));
    if size(vv,2)==1
     bcedg(1,c)=el2ed3(1,i);
     c=c+1;
    end
end
for i=1:size(bcedg,2)
%     E(bcedg(i),bcedg(i))=1;
%     F(bcedg(i),bcedg(i))=1;

    for j=1:r
        if(j~=bcedg(i))
            E(bcedg(i),j)=0;
%                           E(j,bcedg(i))=0;
            F(bcedg(i),j)=0;
%                           F(j,bcedg(i))=0;
        end
    end
end
% % %%
[xv,kz2,iresult]=sptarn(E,F,1,100);
kz=sqrt((kz2));
sol=xv(:,6);
plot(kz,'*')
figure(2); plot(kz,'--rs','LineWidth',2,...
                'MarkerEdgeColor','k',...
                'MarkerFaceColor','r',...
                'MarkerSize',5)
```

```
            xlabel('string')
xlabel({'mode[-]';'Cut off Wave Number for Circular waveguide'})
ylabel('kz')
title('First Orde Edge FEM')

el2no = sort(el2no);
no2xy=p;

% Local coordinates for plotting
phi_1 = [4 3 2 1 0 3 2 1 0 2 1 0 1 0 0]' / 4;
phi_2 = [0 1 2 3 4 0 1 2 3 0 1 2 0 1 0]' / 4;
phi_3 = [0 0 0 0 0 1 1 1 1 2 2 2 3 3 4]' / 4;
% Gradients of the basis functions
edge1 = no2xy(:,el2no(2,:)) - no2xy(:,el2no(1,:));
edge2 = no2xy(:,el2no(3,:)) - no2xy(:,el2no(1,:));
detJ = edge1(1,:).*edge2(2,:) - edge1(2,:).*edge2(1,:);
grad_phi_2x = edge2(2,:)./ detJ;
grad_phi_2y = -edge2(1,:)./ detJ;
grad_phi_3x = -edge1(2,:)./ detJ;
grad_phi_3y = edge1(1,:)./ detJ;
grad_phi_1x = 0 - grad_phi_2x - grad_phi_3x;
grad_phi_1y = 0 - grad_phi_2y - grad_phi_3y;
% Solution values for 1st, 2nd, and 3rd edges in each element
sol1 = sol(el2ed(1,:)).';
sol2 = sol(el2ed(2,:)).';
sol3 = sol(el2ed(3,:)).';
% Field values
Ex=phi_1*( grad_phi_2x.*sol1+grad_phi_3x.*sol2) + phi_2 * (-grad_phi_1x*...
    sol1+grad_phi_3x.*sol3)+phi_3*(-grad_phi_1x.*sol2 - grad_phi_2x.*sol3);
Ey=phi_1*( grad_phi_2y.*sol1+grad_phi_3y.*sol2) + phi_2 * (-grad_phi_1y*...
    sol1+grad_phi_3y.*sol3)+phi_3*(-grad_phi_1y.*sol2 - grad_phi_2y.*sol3);
Hz=(sol1- sol2 + sol3)./detJ;
% subgrid cRATION
p1 = no2xy(:,el2no(1,:));
p2 = no2xy(:,el2no(2,:));
p3 = no2xy(:,el2no(3,:));
psub = kron(p1,phi_1') + kron(p2,phi_2') + kron(p3,phi_3');
% Initiate plotting
ih = ishold;
ax = newplot;
% Plot the curl of the field (constant within each element)
patch('faces',el2no','vertices',no2xy','facevertexcdata',Hz(:), ...
'facecolor',get(ax,'defaultsurfacefacecolor'), ...
'edgecolor',get(ax,'defaultsurfaceedgecolor'));
```

```
axis equal, hold on
% Plot the field itself as arrows
quiver(psub(1,:),psub(2,:),Ex(:)',Ey(:)','k');
% Plot the mesh
xy1 = no2xy(:,el2no(1,:));
xy2 = no2xy(:,el2no(2,:));
xy3 = no2xy(:,el2no(3,:));
xy = [xy1; xy2; xy3; xy1; NaN*xy1];
plot(xy(1:2:end),xy(2:2:end),'k')
% Create a new colormap
mrz = max(abs(Hz(:)));
caxis([-mrz, mrz]);
c = (0:64)'/64; d = [c c ones(size(c))];
colormap([d ;1 1 1; d(end:-1:1,end:-1:1)]);
% if ~ih, hold off,
% %
end


function H = EdgeandNode1orderFEM2D
[no2xy, el2no,noNum,ne]=unimesh01;
x=no2xy(1,:);
y=no2xy(2,:);
t=el2no;
el2no = sort(t);
n1 = el2no([1 1 2],:);
n2 = el2no([2 3 3],:);
[~,~,el2ed] = unique([n1(:) n2(:)],'rows');
el2ed = reshape(el2ed,3,size(el2no,2));
n=el2no';
l=zeros(ne,3);

for e5=1:ne
    l(e5,1)=sqrt((x(n(e5,2))-x(n(e5,1)))^2+(y(n(e5,2))-y(n(e5,1)))^2);
    l(e5,2)=sqrt((x(n(e5,3))-x(n(e5,1)))^2+(y(n(e5,3))-y(n(e5,1)))^2);
    l(e5,3)=sqrt((x(n(e5,3))-x(n(e5,2)))^2+(y(n(e5,3))-y(n(e5,2)))^2);
end
r=max(max(el2ed));
nd=max(max(t));
He=zeros(3,3);
H=zeros(r,nd);
%%%%%%%%%%%%%%%%%%%%%%%% EDGE ELEMENTS CODE %%%%%%%%%%%%%%%%%%%%%%%%
```

```
f=zeros(3,3);
for e6=1:ne
    ii=t(1,e6);
    jj=t(2,e6);
    m=t(3,e6);
    be(1)=y(jj)-y(m);
    be(2)=y(m)-y(ii);
    be(3)=y(ii)-y(jj);
    ce(1)=x(m)-x(jj);
    ce(2)=x(ii)-x(m);
    ce(3)=x(jj)-x(ii);
    Deltae=abs(0.5*(be(1)*ce(2)-be(2)*ce(1)));
    for i=1:3
        for j=1:3

            f(i,j)=(be(i)*be(j)+ce(i)*ce(j));
        end
    end
    He(1,1)=l(e6,1)/(12*Deltae)*(f(2,1)-f(1,1));
    He(1,2)=l(e6,1)/(12*Deltae)*(f(2,2)-f(1,2));
    He(1,3)=l(e6,1)/(12*Deltae)*(f(2,3)-f(1,3));
    He(2,1)=l(e6,2)/(12*Deltae)*(f(3,1)-f(1,1));
    He(2,2)=l(e6,2)/(12*Deltae)*(f(3,2)-f(1,2));
    He(2,3)=l(e6,2)/(12*Deltae)*(f(3,3)-f(1,3));
    He(3,1)=l(e6,3)/(12*Deltae)*(f(3,1)-f(2,1));
    He(3,2)=l(e6,3)/(12*Deltae)*(f(3,2)-f(2,2));
    He(3,3)=l(e6,3)/(12*Deltae)*(f(3,3)-f(2,3));

    for i=1:3
        for j=1:3
            H(el2ed(i,e6),t(j,e6))=H(el2ed(i,e6),t(j,e6))+ He(j,i);
        end
    end
end

%Baundary condition
load('figdata','e');
bcedg=zeros(1,size(e,2));
 el2ed3=el2ed(:)';
 pp=size(el2ed3,2);
 c=1;
for i=1:pp
    [vv,~,~]=find(el2ed3==el2ed3(1,i));
    if size(vv,2)==1
```

```
     bcedg(1,c)=el2ed3(1,i);
     c=c+1;
    end
end
for i=1:size(bcedg,2)
%     H(bcedg(i),bcedg(i))=1;

    for j=1:noNum
        if(j~=bcedg(i))
            H(bcedg(i),j)=0;

        end
    end
end
% % //node boundary condition
ee1=e([1 2],:);
nbc=unique(ee1(:));


for i=1:size(nbc)
    H(nbc(i),nbc(i))=1;

    for j=1:r
        if(j~=nbc(i))
            H(j,nbc(i))=0;

        end
    end
end
end


clc
clear all
close all
[A,B]= nodefirstorderFEM2D;
[M, S, el2ed] =edgFEM2D55;
H =EdgeandNode1orderFEM2D;
eps=1;
k0=1;
miur=1;
Att=1/miur*M-k0^2*eps*S;
Btt=1/miur*S;
```

```
Btz=1/miur*H;
Bzt=Btz';
Bzz=1/miur*A-k0^2*eps*B;
Btt2=Btz*Bzz'*Bzt-Btt;

[xv,kz2,iresult]=sptarn(A,B,1,100);
kz=sqrt((kz2));
% sol=xv(:,75);
% % plot(kz,'*')
figure(1); plot(kz,'--rs','LineWidth',2,...
                'MarkerEdgeColor','k',...
                'MarkerFaceColor','g',...
                'MarkerSize',5)
            xlabel('string')
xlabel({'mode[-]';'Cut off Wave Number'})
ylabel('kz')
title('First Order Node and First Orde Edge FEM')
```